# Combustion and Ignition of Nitramine Propellants: Aspects of Modeling, Simulation, and Analysis

*Eun S. Kim and Vigor Yang*[*]
Department of Mechanical and Nuclear Engineering
The Pennsylvania State University
104 Research Building East, University Park, PA  16802
United States of America

---

[*] Corresponding Author, Email: *vigor@psu.edu*

## TABLE OF CONTENTS

# I. NOMENCLATURE

$A$ = cross-sectional area of propellant sample

$A_g$ = fractional cross-sectional area consisting of gas bubbles in two-phase region

$A_j$ = pre-exponential factor of rate constant of reaction $j$

$A_s$ = interface area between bubbles and liquid per unit volume

$a$ = pre-exponential factor of burning-rate law

$B_j$ = temperature exponent in rate constant of reaction $j$

$C_i$ = molar concentration of species $i$

$c_{pi}$ = constant-pressure specific heat of species $i$

$E_j$ = activation energy of reaction $j$

$e$ = internal energy

$H_v$ = enthalpy of vaporization

$h$ = enthalpy

$h_c$ = heat transfer coefficient

$h_i$ = static enthalpy of species $i$

$h_{f_i}^{\circ}$ = heat of formation of species $i$ at standard condition

$k_j$ = rate constant of reaction $j$

$\dot{m}''$ = mass flux

$N$ = total number of species

$n$ = pressure exponent

$N_R$ = total number of reactions

$p$ = pressure

$p_0$ = pre-exponential factor of vapor pressure in Arrhenius form

$\dot{Q}''_{\text{laser}}$ = laser heat flux

$r_b$ = propellant burning rate

$R_u$ = universal gas constant

$T$ = temperature

$s$ = sticking coefficient

$t$ = time

$u$ = bulk velocity

$V_i$ = diffusion velocity of species $i$

$\bar{v}_n$ = average normal velocity component of vapor molecule

$W_i$ = molecular weight of species $i$

$\dot{w}_i$ = mass production rate of species $i$

$\dot{w}_{Rj}$ = mass production rate of reaction $j$

$X_i$ = molar fraction of species $i$

$x$ = spatial coordinate

$Y_i$ = mass fraction of species $i$

### *Greek Symbols*

$\phi$ = void fraction

$\rho$ = density

$\lambda$ = thermal conductivity

$\dot{\omega}$ = molar production rate

### *Subscripts*

$0^+$ = gas-phase side of propellant surface

$0^-$ = condensed-phase side of propellant surface

$c$ = condensed phase

$c{-}g$ = from condensed to gas phase

cond = condensation

eq = equilibrium condition

evap = evaporation

$f$ = mass-averaged quantity in subsurface foam layer

$g$ = gas phase

$i$ = preconditioned state

$l$ = liquid phase

$s$ = propellant surface or solid phase

$v$ = vapor

# II. INTRODUCTION

This chapter deals with the state-of-the-art theoretical modeling and numerical simulation of steady-state combustion and laser-induced ignition of nitramine monopropellants, including cyclotrimethylenetrinitramine (RDX) and cyclotetramethylenetetranitramine (HMX), as well as steady-state combustion of RDX/glycidyl azide polymer (GAP) and HMX/GAP pseudo-propellants. The prefix pseudo is used to emphasize that RDX (or HMX) and GAP are mixed physically and no curing agent is used as for operational propellants. These energetic compounds, with their molecular structures shown in Figure 1, have been widely used in many propulsion and gas-generation systems to meet various stringent performance and environmental requirements. They are highly energetic and produce high impetus and specific impulse for gun and rocket propulsion applications. In comparison with ammonium perchlorate (AP), nitramines produce little smoke, toxicity, and corrosion. Azide-containing energetic binders, such as GAP, 3,3-bis(azidomethly)oxetane (BAMO), and 3-azidomethyl-3-methyloxetane (AMMO), have positive heats of formation but produce relatively low-temperature flames.

In the past decade, significant progress has been made in the study of combustion-wave structures and ignition characteristics of RDX and HMX monopropellants. Extensive experimental diagnostics[1-23] and theoretical analyses[24-40] were conducted over a broad range of operating conditions. Both self-sustained and laser-assisted combustion[24-39], as well as ignition transients[39,40], have been treated in detail. Studies on the physical properties, sublimation, decomposition, ignition, and self-deflagration of nitramine propellants conducted prior to 1984 are summarized by Boggs[41] and Fifer[42], and the state of understanding of steady-state combustion of nitramine propellants up to 1990 is given by Alexander *et al*.[43]. Recently, Brill *et al*. provides a comprehensive overview of various studies on the near-surface chemical kinetics of RDX and HMX [5]. A summary of the overall latest development is covered in a volume edited by Yang *et al.* [44].

Most of early theoretical analyses of steady-state combustion of nitramine propellants were based on global reaction schemes for gas-phase processes[45]. The first comprehensive model of RDX combustion, accommodating 23 species and 49 reactions in the gas phase, was initiated by Ermolin *et al.*[46]. The propellant surface conditions, however, were treated as input parameters in order to match experimentally measured species-concentration profiles. A substantial improvement was made by Melius[24] to relax this constraint. His formulation simultaneously took into account the thermal decomposition of RDX and the ensuing chemical reactions to an extent that the key heat-release mechanisms could be identified. Yetter *et al.*[25] refined Melius' model to include the sub-models of reactions among the major intermediate products such as $CH_2O$, $NO_2$, $N_2O$, $H_2$, HCN, and NO, but a significant amount of uncertainties still existed about the pathways of the reduction and associated rates of large fragments departing from the burning surface of these cyclic nitramines. By considering global reactions, Margolis, Williams, Li, and co-workers[26-28] developed an analytical approach, which included the presence of gas bubbles and liquid droplets in the two-phase region near the propellant surface by means of methods of matched asymptotic expansion. The model, however, provided limited information concerning the chemical processes. Prasad *et al.* also studied self-sustained and laser-assisted combustion of RDX and HMX[29,30]. Their model differed from the ones described in References 24-28 in that bubble formation within the liquid layer was neglected. In general, these models of RDX and HMX combustion predicted burning rate, surface temperature, and melt-layer thickness reasonably accurately, although some disagreements with experimental data in the near-surface species profiles and the temperature sensitivity of propellant burning rate were noted. Recognizing the important role of the condensed phase, Liau and Yang developed a detailed model of RDX combustion accounting for the foam layer, which is the region between the gas and solid phases[32,33]. Such a foam layer consisted of two phases: liquefied RDX and bubbles containing gaseous RDX and its decomposition products. Davidson and Beckstead[34] further studied the near-surface temperature distribution and pressure sensitivity of burning rate. In the past decade, extensive studies have been conducted to study the chemical kinetics of the near-surface region of RDX and HMX. The similar approach was later extended to study the combustion behavior of HMX[35]. The recent studies have provided great insight into the underlying mechanisms dictating the chemistry of the subsurface region as well as near-surface gas phase. However, more needs to be learned about complex processes involved in the two-phase near-surface region, which includes an array of intricacies such as thermal decomposition, subsequent reactions, evaporation, bubble formation and interaction, and interfacial transport of mass and energy between the gas and condensed phases. An integrated modeling and experimental effort is required to improve the state of knowledge.

Similar to the steady-state combustion model development, a series of theoretical ignition modeling efforts has also been carried out in the past to study the ignition behavior of solid propellants and explosives. A comprehensive review of the early work was conducted by Price *et al.* in 1966[47]. The experimental and theoretical literature pertaining to the ignition of solid propellants over the period of 1966 through 1980 was reviewed by Kulkarni *et al.*[48] and Hermance[49]. The state of understanding in Russia up to 1989 was presented by Vilyunov and Zarko[50], giving a detailed examination of the various ignition models and related experimental approaches. In 1998, a review of laser and radiative ignition of 24 solid energetic materials, with emphasis on work performed in the Former Soviet Union, was provided by Strakouskiy *et al.*[51].

Ignition of solid propellants and explosives involves an array of intricate physiochemical processes under energetic stimuli, and has been a subject of extensive research since 1950. In general, ignition models can be broadly divided into four categories: solid-phase (or reactive solid), heterogeneous, gas-phase, and multi-phase reaction models. The solid-phase reaction models[52-55] assume that exothermic reactions in the condensed phase are the dominant mechanism of ignition, while the effects of surface and gas-phase processes are secondary and can be neglected. Heterogeneous reaction models[56-64] assume that heterogeneous reactions at the propellant surface are responsible for ignition due to the molecular diffusion of ambient oxidizer species to the propellant surface. The gas-phase reaction models[65-72] presume that exothermic gas-phase reactions and their heat feedback to the propellant surface are the primary mechanism of ignition. In spite of their contributions in correlating experimental data and providing qualitative understanding of ignition behavior, the solid-phase (or reactive solid), heterogeneous, and gas-phase reaction models[52-72] are semi-empirical in nature and do not provide predictive capability at scales sufficient to resolve the detailed ignition mechanisms and flame evolution. A prior understanding of the ignition process is usually required before modeling. This obstacle mainly results from the use of global kinetics schemes derived for steady-state combustion. Moreover, a simple pyrolysis law is often employed to describe the propellant gasification process in terms of propellant surface temperature along with prescribed condensed-phase heat release. Recently, Yang and coworkers developed a multi-phase reaction model by extending the steady-state model described in References 32 and 33 to include the transient development in the entire combustion zone, including the solid-phase, near-surface two-phase, and gas-phase regions[39,40]. The formulation accommodates detailed chemical kinetics and transport phenomena in the gas-phase region, as well as thermal decomposition and subsequent reactions in the two-phase region. Thermodynamic phase transition and volumetric radiant energy absorption are also considered for a complete description. The model is capable of treating the entire ignition process from surface pyrolysis to steady-state combustion, with the instantaneous burning rate and surface conditions treated as part of the solution[39,40]. A summary of the theoretical formulation and results of this multi-phase model is given in the following sections of the current chapter.

Unlike the situation with nitramine monopropellants, limited theoretical modeling studies for GAP decomposition and combustion are available[37-38, 73]. More effort, however, has been expended on experimental studies[3, 74-80]. The entire combustion-wave structure can be segmented into three regions: solid-phase, near-surface two phase, and gas-phase regimes. In the solid phase, the extent of chemical reactions is usually negligible due to the low temperature and short residence time. Thermal decomposition and ensuing reactions, as well as phase transition, take place in the foam layer, generating gas bubbles and forming a two-phase region. Rapid gasification occurs at the burning surface, and further decomposition and oxidation continue to take place and release a significant amount of energy in the near-surface region. The burning surface temperature is greater than 700 K. No visible flame is observed in the gas phase; instead, a large amount of fine powder is formed away from the burning surface and generates a cloud of intense smoke. The final flame temperature of GAP is around 1300-1500 K, which is significantly lower than those of nitramines (~ 3000 K).

Recently, gas-phase species and temperature measurements were conducted to investigate $CO_2$ laser-induced pyrolysis of cured GAP at the intensities of 100 and 200 $W/cm^2$ under atmospheric pressure using a triple quadrupole mass spectrometer (TQMS) with fine-wire thermocouples[74]. The decomposition products observed in that work were $N_2$, HCN, CO, $H_2CO$, $NH_3$, $CH_3CHO$, $CH_2CHCHNH$, $CH_3CHNH$, $H_2O$, $CH_4$, and $C_2H_4$. Among these, the major species were $N_2$, HCN, CO, and $H_2CO$. The relative concentrations of these decomposed species were similar to those observed by Arisawa and Brill[75]. Very intense smoke was formed in the gas phase; no carbonaceous residue was observed on the burning surface. The smoke formation was thus assumed to be caused by cold ambient gases, quenching hot condensable gases issuing from the GAP surface. The surface temperature was measured to be 1050 K under both heat fluxes of 100 and 200 W/cm$^2$, which is considerably higher than those reported in the literature (References 76-78) ($T_s$ = 700-760 K, 710-750 K, and 813 K) possibly due to differences in sample preparation (cured vs. uncured GAP), experimental conditions (self-sustained vs. laser-assisted combustion), type of GAP strands used, diagnostic technique, and measurement accuracy. Both the surface temperature and the burning rate of GAP were higher than those of HMX under the same experimental condition. Using TQMS with fine-wire thermocouples, Litzinger *et al.*[3] also conducted gas-phase species and temperature measurements to study the combustion characteristics of several nitramine/azide pseudo-propellants including RDX/GAP and HMX/GAP, all with a mass ratio of 8:2. The experiments were performed at $CO_2$ laser heat fluxes of 100-400 W/cm$^2$ under atmospheric pressure. Emphasis was placed on the effects of nitramine/azide interaction and external heat flux. The major decomposition species for HMX/GAP and RDX/GAP were similar to those found for neat HMX and RDX. The species-concentration profiles showed three distinct regions: a primary reaction zone, a dark zone, and a secondary reaction zone. The burning rates of HMX/GAP and RDX/GAP were increased with the addition of GAP, regardless of the laser energy intensity impressed. This finding contradicted the experimental results obtained by Kubota and Sonobe[76], which showed that the addition of GAP into HMX lowered the burning rate. The discrepancy may arise from the differences in their experimental setups and sample preparation. For instance, the HMX used by Kubota and Sonobe[76] had a bimodal particle size distribution (70% of 2 μm and 30% of 20 μm), compared with an average crystal size of 75 μm used by Litzinger *et al.*[3]. Furthermore, the GAP was cured with hexamethylene diisocyanate (HMDI) and crosslinked with trimethylolpropane (TMP) in Kubota and Sonobe's experiments. The T-jump/FTIR spectroscopy technique was applied to the study of the decomposition characteristics of GAP having one, two, and three terminal –OH groups[75]. Samples were rapidly heated to a temperature range of 500-600 K at 2 atm with a heating rate of 800 K/s. The major decomposition products were $CH_4$, HCN, CO, $C_2H_4$, $NH_3$, $CH_2O$, $CH_2CO$, $H_2O$, and GAP oligomer. IR-inactive $N_2$ was not measured, but is present as one of the major decomposition products of GAP in other studies using mass spectrometry[74,79]. $NH_3$ was found to be formed from the end chain of the azide group. The formation of CO appeared to result from both the parent polymer and secondary reactions. The ratio of HCN to $NH_3$ increased as temperature increased. The intensive heat release during GAP decomposition explains the high burning surface temperature of GAP[74].

Over the past several years, Yang and coworkers[37-39] have established comprehensive numerical analyses of nitramine/GAP pseudo-propellant combustion to predict the propellant burning rate and detailed combustion wave structure over a broad range of pressure, laser intensity, and propellant composition. The steady-state model described in References 32 and 33 was extended to include GAP binder in the nitramine combustion. The model takes into account various fundamental processes at scales sufficient to resolve the microscopic flame-zone physiochemistry. The thermochemical parameters of nitramine and GAP are deduced from existing experimental data. Four global decomposition reactions in the condensed phase as well as subsequent reactions are included. In the gas phase, a detailed chemical kinetics scheme involving 74 species and 532 reactions is employed to describe the heat-release mechanism. The key physiochemical processes dictating the propellant burning behavior and flame structure were studied over a broad range of ambient pressure, preconditioned temperature, propellant composition, and impressed laser intensity.

In the following sections, the combustion-wave structures and burning characteristics of RDX[32,33,39,40], HMX[39], HMX/GAP[37,39], and RDX/GAP[38] will be briefly discussed. The state-of-the-art approaches recently developed in this subject area are then described along with a brief discussion of the numerical techniques. Finally, results of these modeling studies are summarized.

# III. DESCRIPTION OF COMBUSTION-WAVE STRUCTURES

Three physical problems are considered in this chapter: 1.) steady-state combustion of nitramine propellants; 2.) laser-induced ignition of RDX monopropellant; and 3.) steady-state combustion of nitramine/GAP pseudo-propellants. During the past decade, Yang and co-workers [32,33,36-40] have developed a series of comprehensive numerical models for studying the key physiochemical processes involved in the combustion and ignition of nitramine monopropellant and nitramine/GAP pseudo-propellants. These models accommodated detailed chemical kinetics and transport phenomena in the gas phase, as well as thermal decomposition and subsequent reactions in the condensed phase. The formation of gas bubbles in the molten surface layer due to molecular degradation and thermodynamic phase transition is also included to provide a complete description. The steady-state combustion models[32,33,36-39] are capable of resolving the combustion-wave structures in both the gas and condensed phases, with the instantaneous burning rate and surface temperature calculated as part of the solution. The analyses[32,33] were later extended to treat the entire ignition process from surface pyrolysis to steady-state combustion[39,40].

## *A. Steady-State Combustion of RDX Monopropellant*

Figure 2 shows the physical model of concern, a strand of RDX monopropellant burning in a stagnant environment with or without the assistance of external laser heat flux. To facilitate formulation, the entire combustion-wave structure is conveniently segmented into three regions: 1.) solid phase; 2.) near-surface two phase, and 3.) gas phase. During burning, the propellant remains thermally stable in the solid phase until the temperature approaches the melting point at which thermodynamic phase transition occurs as shown in Figure 3. Molecular degradation and evaporation of RDX then take place in the liquid layer, generating bubbles and forming a two-phase region. The propellant subsequently undergoes a sequence of rapid evaporation and decomposition in the near field immediately above the foam layer. Oxidation reactions continue to occur and to release an enormous amount of energy in the gas phase, with the final temperature reaching the adiabatic flame temperature. A detailed description of the theoretical model can be found in References 32 and 33.

### *B. Laser-Induced Ignition of RDX Monopropellant*

The physical problem of concern is the ignition of a strand of RDX monopropellant induced by a continuous and radially uniform $CO_2$ laser. The physiochemical processes involved are schematically illustrated in Figure 4. The propellant and the ambient gas are initially at room temperature. Once the laser is activated, volumetric absorption of laser energy in the solid phase takes place, as shown in Figure 4a. In the gas phase, only certain gaseous species, such as vapor RDX, absorb a noticeable amount of laser energy at the wavelength of 10.6 μm; thus, the gas-phase absorption is negligible during the inert heating period. When the solid reaches its melting temperature, the absorbed radiant energy can not further raise the temperature without first melting the solid. Since the radiant energy absorbed is insufficient for instantaneous melting of all of the solid in a short period, partial melting of the solid occurs, which leads to the formation of a mushy zone consisting of both solid and liquid (Figure 4b). When a pure liquid layer is formed, the solid-liquid interface starts to move due to conductive and radiative heat transfer (Figure 4c). In the liquid, thermal decomposition and subsequent reactions, as well as phase transition, take place, generating gas bubbles and forming a two-phase region. The propellant then undergoes a sequence of rapid evaporation at the surface (Figure 4d). Ignition occurs if the heat flux is sufficiently large to initiate the subsequent self-accelerated exothermic reactions which result in substantial heat release (in the gas phase) and emission of light. A luminous flame is produced, regresses toward the surface, and finally reaches a stationary position corresponding to its steady-state condition. A comprehensive description of the theoretical model is given in References 39 and 40.

### *C. Steady-State Combustion of Nitramine/GAP Pseudo-Propellants*

Figure 5 shows schematically the physiochemical processes involved in the HMX/GAP pseudo-propellant combustion. A physical model for RDX/GAP pseudo-propellant combustion is available in Reference 38. The entire combustion-wave structure is segmented into three regions: solid phase, near-surface two phase, and gas phase. In the solid-phase region, HMX powder and GAP are physically mixed. The former melts at 558 K with negligible chemical reactions taking place, due to the low temperature and short residence time. Thermal decomposition and phase change of HMX occurs in the liquid phase to form a foam layer. The propellant surface ($x = 0$) is defined herein as the interface between the foam layer and gas-phase region, at which rapid gasification of HMX prevails. Since the surface temperature of HMX/GAP pseudo-propellant (~700 K) is lower than that of pure GAP, GAP leaves the surface as aerosol surrounded with vapor HMX and its decomposed gaseous products. In this region, GAP remains as a condensed species and continues to decompose. A significant amount of carbonaceous residue may be present on the surface during combustion. To facilitate analysis, the coordinate system is fixed at the propellant surface. A quasi one-dimensional model is formulated as a first approximation of the problem. Both the sub-surface and near-surface regions require a multi-phase treatment because of the presence of GAP and other condensed species in these zones. A detailed derivation of the theoretical model is available in References 37 and 39. A similar model approach has been applied for studying RDX/GAP pseudo-propellant combustion[38].

## IV. THEORETICAL FORMULATION

The theoretical formulation of physiochemical processes in various regions during the ignition and combustion of HMX/GAP pseudo-propellant is summarized below[37]. For monopropellants, the model can be simplified by removing the GAP terms in the following governing equations and are described in References 32, 33, 39, and 40. The steady-state combustion can be treated as a limiting case by neglecting all the time-varying terms.

### *A. Solid-Phase Region*

Thermal decomposition of HMX and GAP and in-depth radiation absorption are ignored in modeling the solid-phase process. Thus, only heat conduction governed by the following equation is considered:

$$\rho_c c_c \frac{\partial T_c}{\partial t} + \rho_c u_c c_c \frac{\partial T_c}{\partial x} = \frac{\partial}{\partial x}\left( \lambda_c \frac{\partial T_c}{\partial x} \right) \tag{1}$$

The thermal conductivities and specific heat capacities of solid HMX and liquid GAP were recently obtained as a function of temperature by Hanson-Parr and Parr[17]. Measurements of these properties for liquid HMX, however, represent a much more challenging task, because decomposition usually takes place before the melting. Thus, they are assumed to be identical to those at the solid state due to the lack of reliable data. The thermodynamic and transport properties used in the present work are given in Reference 37. The properties of the mixture are estimated as follows.

$$\rho_c c_c = Y_{\mathrm{HMX}} \rho_{\mathrm{HMX}} c_{\mathrm{HMX}} + Y_{\mathrm{GAP}} \rho_{\mathrm{GAP}} c_{\mathrm{GAP}} \tag{2}$$

$$\lambda_c = Y_{\mathrm{HMX}} \lambda_{\mathrm{HMX}} + Y_{\mathrm{GAP}} \lambda_{\mathrm{GAP}} \tag{3}$$

A closed-form solution to Equation (1) at steady state is available subject to appropriate boundary conditions and the propellant burning rate.

## *B. Subsurface Multi-Phase Region*

The physiochemical processes in this region are extremely complex, involving an array of intricacies such as thermal decomposition, evaporation, bubble formation, gas-phase reactions in bubbles, and interfacial transport of mass and energy between the gas and condensed phases. A two-phase fluid dynamic model based on a spatial averaging technique is employed to formulate these complicated phenomena[32]. With the assumption that mass diffusion is negligible, the conservation equations for both the condensed and gas phases can be combined and written as follows.

*Mass*

$$\frac{\partial[(1-\phi_f)\rho_c+\phi_f\rho_g]}{\partial t}+\frac{\partial}{\partial x}[(1-\phi_f)\rho_c u_c+\phi_f\rho_g u_g]=0, \tag{4}$$

*Condensed Species Concentration*

$$\frac{\partial[(1-\phi_f)\rho_c Y_{c_i}]}{\partial t}+\frac{\partial}{\partial x}[(1-\phi_f)\rho_c u_c Y_{c_i}]=\dot{w}_{c_i} \quad (i=1,2,...,N_c), \tag{5}$$

*Gaseous Species Concentration*

$$\frac{\partial(\phi_f\rho_g Y_{g_i})}{\partial t}+\frac{\partial(\phi_f\rho_g u_g Y_{g_i})}{\partial x}=\dot{w}_{g_i} \qquad (i=1,2,...,N_g), \tag{6}$$

*Energy*

$$\begin{aligned}\rho_f c_f\frac{\partial T_f}{\partial t}-\frac{\partial p}{\partial t}+\rho_f u_f c_f\frac{\partial T_f}{\partial x}&=\frac{\partial}{\partial x}\left(\lambda_f\frac{\partial T_f}{\partial x}\right)-\sum_{j=1}^{N_g}\dot{w}_{gj}h_{gj}-\sum_{j=1}^{N_g}\dot{w}_{cj}h_{cj}\\&+\sum_{j=1}^{N_g}h_{gj}Y_{gj}\dot{w}_{c-g}-\sum_{j=1}^{N_c}h_{cj}Y_{cj}\dot{w}_{c-g}\end{aligned} \tag{7}$$

where $\dot{w}_{c-g}$ represents the rate of mass conversion from liquid to gas. The properties are mass-averaged as follows.

$$\rho_f c_f = \left(1-\phi_f\right)\rho_c c_c + \phi_f \rho_g c_g , \tag{8}$$

$$\rho_f u_f c_f \equiv \left(1-\phi_f\right)\rho_c u_c c_c + \phi_f \rho_g u_g c_g , \tag{9}$$

$$\lambda_f = \left[\left(1-\phi_f\right)\rho_c u_c \lambda_c + \phi_f \rho_g u_g \lambda_g\right] / \left[\left(1-\phi_f\right)\rho_c u_c + \phi_f \rho_g u_g\right] \tag{10}$$

where

$$c_c = \sum_{i=1}^{N_c} c_{c_i} Y_{c_i}\ ,\ c_g = \sum_{i=1}^{N_g} c_{g_i} Y_{g_i}\ ,\ \lambda_c = \sum_{i=1}^{N_c} \lambda_{c_i} Y_{c_i}\ ,\ \text{and}\ \lambda_g = \sum_{i=1}^{N_g} \lambda_{g_i} Y_{g_i} \tag{11a-d}$$

The mass and energy production terms depend on the specific chemical reaction mechanisms used and can be formulated as described below.

The model accommodates the thermal decomposition of HMX and GAP, as well as subsequent reactions in the foam layer. The formation of gas bubbles due to evaporation and thermal degradation is also considered for completeness. Two global-decomposition pathways are employed for HMX, as listed in Table 1. The first reaction (R1) is an exothermic, low-temperature pathway, whereas the second reaction (R2) is an endothermic, high-temperature pathway. Unfortunately, uncertainties still exist about the kinetic rates of (R1) and (R2). A parametric study is thus performed to assess the role of the condensed-phase kinetics of HMX in the overall combustion process of HMX/GAP pseudo-propellant. Two different sets of rates are available in the literature for (R1) and (R2): one estimated by Davidson and Beckstead[34] using their combustion model and the other obtained by Brill[12] from the T-jump/FTIR experiment. Subsequent reactions among the products of (R1) and (R2) may occur to provide the thermal energy to sustain pyrolysis. Brill[12] examined several plausible secondary reactions and their reaction rates. Results indicate that reaction (R6) between $CH_2O$ and $NO_2$ is probably the most important one in the foam layer if it indeed does occur. The rate parameter of reaction (R6) was determined with shock-tube experiments[16]. Thermodynamic phase transition consisting of both evaporation and condensation of HMX, (R5), is considered to provide a complete description of the mass transfer process.

The GAP sample considered in the present study is composed of 56 monomer units and is denoted "GAP56." A global, condensed-phase decomposition mechanism for GAP was established based on the experimental data reported in[74, 75, 81]. There is universal agreement that GAP decomposition is initiated by the bond cleavage of the azide group releasing $N_2$[74-80]. This process proceeds rapidly over a temperature range from 260 to 290 °C, and has an activation energy of about 41 kcal/mol[75]. There are, however, uncertainties as to how the bond breaking process occurs. We assume a first-order reaction with the pre-exponential factor and activation energy deduced by Sysak *et al.*[81], as given by reaction (R3) in Table 1.

The subsequent step in the decomposition of GAP releases $NH_3$. Its concentration in the gas phase increases with increasing number of –OH end groups in the polymer. It appears that H-atom abstraction involving the –OH end group is an important channel for $NH_3$ formation. At this time, there are no mechanistic details which allow one to quantify the $NH_3$ evolution as a global reaction, and thus a rate expression cannot be formulated. Since $NH_3$ is an important source for H-atoms in the gas phase, the deficiency in predicted species concentrations caused by neglecting this step in the decomposition of GAP must be noted. Finally, a rapid, highly exothermic event takes place and releases HCN, CO, $CH_2O$, $CH_2CO$, $CH_4$, $C_2H_4$, $H_2O$, and GAP oligomers, in addition to $NH_3$[75].

In the laser-assisted combustion study of GAP polyol by Tang *et al.*[74], the surface temperature approached 1050 K, which was about 400 K higher than those treated by Arisawa and Brill[75]. Because of this higher temperature, Tang *et al.*[74] identified several different large molecular species using TQMS. The major ones were acetaldehyde ($CH_3CHO$), acrolein ($C_2H_3CHO$), and different imines ($CH_3CHNH$ and $CH_2CHCHNH$). In comparing the results of Arisawa and Brill[75] with those of Tang *et al.*[74], it appears that the GAP oligomers identified by Arisawa and Brill are likely candidates to form the imines identified by Tang *et al.* A species balance of the data acquired by

Tang *et al.*[74] leads to a global reaction model for the decomposition of GAP56*, which is the polymer unit that has released $N_2$, as given by reaction (R4) in Table 1.

Most of the gaseous decomposition products from GAP are hydrocarbons or common gases whose chemical kinetic details are readily available. However, the available information about aldehydes ($CH_3CHO$ and $C_2H_3CHO$) and imines ($CH_3CHNH$ and $CH_2CHCHNH$), as well as their interactions with either HMX or its decomposition products, appears to be limited. To allow for a reduction of these species, bimolecular decomposition reactions have been formulated, with the activation energies about the differences in enthalpy between products and reactants[38]. The pre-exponential factors are assigned values that are typical for such a process. The reactions considered are listed as reactions (R7-R10) in Table 1.

Note that the condensed species $GAP56_{(l)}$, $GAP56^{*}_{(l)}$, and $C_{(s)}$ are dissolved in liquid HMX, whereas all other species are gaseous and exist in bubbles. Based on the chemical mechanism given by (R1-R6), the species production terms in Equations (5) and (6) can be expressed and are listed explicitly in References 37 and 39.

## *C. Gas-Phase Region*

The species evolved from the propellant surface into the gas phase include vapor HMX, decomposition products of HMX and GAP, and unreacted GAP. Since condensed and gaseous species both exist in this region, a two-phase treatment similar to that described in the preceding section is employed to formulate the problem. The effect of laser absorption in the gas phase on the ignition and combustion processes of nitramine monopropellants has been extensively investigated in Reference 40. Results indicate that only vapor RDX may absorb an appreciable amount of $CO_2$ laser energy in the gas phase. None of the major gaseous decomposition products of RDX exhibits a noticeable absorption at a wavelength of 10.6 μm of $CO_2$ laser. Thus the fraction of the laser energy absorbed in the gas phase appears quite limited (less than 10%). The heat release from exothermic reactions is much more pronounced than the laser energy absorbed by the gas phase. The same argument applies to HMX as well since the decomposition species of HMX and RDX are similar

With the assumption that body force, viscous dissipation, and radiation emission/absorption effects are ignored, the isobaric conservation equations for both the condensed and gas phases can be combined and written as follows.

*Mass*

$$\frac{\partial[(1-\phi_g)A\rho_c+\phi_g A\rho_g]}{\partial t}+\frac{\partial}{\partial x}[(1-\phi_g)A\rho_c u_c+\phi_g A\rho_g u_g]=0, \tag{12}$$

*Condensed Species Concentration*

$$\frac{\partial[(1-\phi_g)A\rho_c Y_{c_i}]}{\partial t}+\frac{\partial}{\partial x}[(1-\phi_g)A\rho_c u_c Y_{c_i}]=A\dot{w}_{c_i} \qquad (i=1,2,...,N_c), \tag{13}$$

*Gaseous Species Concentration*

$$\begin{aligned}\phi_g A\rho_g\frac{\partial Y_{g_i}}{\partial t}+\phi_g A\rho_g u_g\frac{\partial Y_{g_i}}{\partial x}+\frac{\partial(\phi_g A\rho_g V_{gi}Y_{g_i})}{\partial x}&=A\dot{w}_{g_i}\\ -Y_{gi}A\dot{w}_{c-g}&\qquad\qquad (i=1,2,...,N_g),\end{aligned} \tag{14}$$

*Energy*

$$\begin{aligned}\rho c_p A\frac{\partial T_g}{\partial t}-\frac{\partial(pA)}{\partial t}+\rho u c_p A\frac{\partial T_g}{\partial x}=\frac{\partial}{\partial x}\left(\lambda A\frac{\partial T_g}{\partial x}\right)&-\phi_g A\sum_{j=1}^{N_g}\rho_g Y_{g_i}V_{g_i}c_{p_{g_i}}\frac{\partial T_g}{\partial x}\\ &-A\sum_{j=1}^{N_g}\dot{w}_{g_j}h_{gj}-A\sum_{j=1}^{N_c}\dot{w}_{cj}h_{cj}+A\sum_{j=1}^{N_g}h_{gj}Y_{gj}\dot{w}_{c-g}\\ &-A\sum_{j=1}^{N_c}h_{cj}Y_{cj}\dot{w}_{c-g},\end{aligned} \tag{15}$$

The thermophysical properties used in Equation (15) are mass-averaged as follows.

$$\rho c_p=(1-\phi_g)\rho_c c_c+\phi_g\rho_g c_g, \tag{16}$$

$$\rho u c_p=(1-\phi_g)\rho_c u_c c_c+\phi_g\rho_g u_g c_g, \tag{17}$$

$$\lambda_g = \left[ (1-\phi_g)\rho_c u_c \lambda_c + \phi_g \rho_g u_g \lambda_g \right] / \left[ (1-\phi_g)\rho_c u_c + \phi_g \rho_g u_g \right] \tag{18}$$

The enthalpy of gaseous or condensed species *i* in Equation (15) is defined as

$$h_i = \int_{T_{ref}}^{T} c_{p_i} dT + h_{f_i}^{\circ} \tag{19}$$

The mass diffusion velocity $V_i$ consists of contributions from both concentration and temperature gradients,

$$V_i = -D_i \frac{1}{X_i} \frac{\partial X_i}{\partial x} + D_i \frac{D_{T_i}}{X_i} \frac{1}{T} \frac{\partial T}{\partial x} \tag{20}$$

Finally, the equation of state for a multi-component system is used to close the formulation.

$$p = \rho_g R_u T_g \sum_{i=1}^{N_g} \frac{Y_{g_i}}{W_{g_i}} \tag{21}$$

The chemical reactions can be written in the following general form

$$\sum_{i=1}^{N_g} \nu'_{ij} M_i \underset{k_{bj}}{\overset{k_{fj}}{\Leftrightarrow}} \sum_{i=1}^{N_g} \nu''_{ij} M_i, \quad j = 1, 2, ..., N_R \tag{22}$$

where $\nu'_{ij}$ and $\nu''_{ij}$ are the stoichiometric coefficients for the *i*th species appearing as a reactant in the *j*th forward and backward reactions, respectively, and $M_i$ is the chemical symbol for the *i*th species. The reaction rate constant $k_j$ (either $k_{fj}$ or $k_{bj}$ ) is given by the Arrhenius expression

$$k_j = A_j T^{B_j} \exp(-E_j / R_u T) \tag{23}$$

The rate of change of molar concentration of species *i* by reaction *j* is

$$\dot{C}_{ij} = (\nu'_{ij} - \nu''_{ij})(k_{fj} \prod_{i=1}^{N_g} C_i^{\nu'_{ij}} - k_{bj} \prod_{i=1}^{N_g} C_i^{\nu''_{ij}}) \tag{24}$$

The total mass production rate of gaseous species *i* in Equation (14) is then obtained by summing up the changes due to all gas- and condensed-phase reactions:

$$\dot{w}_{g_i} = \phi_g W_{g_i} \sum_{j=1}^{N_R} \dot{C}_{ij} + \dot{w}_{c-g,g_i} \tag{25}$$

where $\dot{w}_{c-g,g_i}$ represents the mass conversion rate from liquid to gas of gaseous species *i*.

The gas-phase chemical kinetics scheme is composed of four submodels: 1.) the HMX combustion mechanism[30], 2.) the additional reactions, recently proposed by Chakraborty and Lin[4], involving the consumption of $H_2CNNO_2$, $H_2CNNO$, $H_2CNO$, $H_2CNOH$, and $H_2CN$, 3.) the initial decomposition reactions of GAP including, among others, aldehydes and imines, and 4.) the hydrocarbon combustion mechanism[82] containing 49 species and 279 reactions. Bimolecular decomposition reactions for the aldehydes ($CH_3CHO$ and $C_2H_3CHO$) and imines ($CH_3CHNH$ and $CH_2CHCHNH$) are assumed, and their kinetic rates are estimated, as indicated by reactions (R7-R10) in Table 1. In total, the gas-phase chemical kinetics scheme involves 74 species and 532 reactions.

The mass production rates of species generated by condensed-phase reactions in Equations (13) and (14) are described by reactions (R3) and (R4) of condensed species such as GAP and its intermediate product. The rate expressions of reactions listed in References 37-39 are utilized to calculate the mass production rates of species generated from GAP decomposition in the gas phase.

## *D. Boundary Conditions*

The physical processes in the gas phase and foam layer must be matched at the propellant surface to provide the boundary conditions for each region. This procedure requires balances of mass and energy, and eventually determines propellant surface conditions and burning rate. With the neglect of mass diffusion in the condensed phase, the conservation laws at the propellant surface can be written as follows.

*Mass*

$$\left[\left(1-\phi_f\right)\rho_c u_c+\phi_f\rho_g u_g\right]_{0^-}=\left[\left(1-\phi_g\right)\rho_c u_c+\phi_g\rho_g u_g\right]_{0^+} \tag{26}$$

*Species*

$$\left[(1-\phi_f)\rho_c u_c Y_{c_i} + \phi_f \rho_g u_g Y_{g_i}\right]_{0^-} = \left[(1-\phi_g)\rho_c u_c Y_{c_i} + \phi_g \rho_g (u_g + V_{g_i}) Y_{g_i}\right]_{0^+} \tag{27}$$

*Energy*

$$\left[\lambda_f \frac{dT_f}{dx} + (1-\phi_f)\rho_c u_c Y_{\mathrm{HMX}_c} h_{\mathrm{HMX}_{l\to g}}\right]_{0^-} = \left[\lambda_g \frac{dT_g}{dx}\right]_{0^+} + \dot{Q}''_{\mathrm{laser}} \tag{28}$$

The temperature is identical on both sides of the interface, but the void fraction and species mass fractions might be different. The treatment of surface absorption of incident radiative energy, $\dot{Q}''_{laser}$, is given in Reference 40.

Since the propellant surface is defined as the interface where rapid phase transition occurs, the evaporation law of HMX is assumed to prevail at the interface[32, 33, 37-40], giving

$$\left[(1-\phi_f)\rho_c u_c Y_{\mathrm{HMX}_c}\right]_{0^-} = \left[s\bar{v}_n C_{\mathrm{HMX}_g}\left(\frac{p_{v,\mathrm{eq}}}{p} - X_{\mathrm{HMX}_g}\right)\right]_{0^+} \tag{29}$$

It has been shown that $\rho_c u_c = \rho_g u_g$ is a good assumption for the two-phase model[32, 33, 37-40]. Equation (26) becomes trivial and Equation (27) can be written as follows.

$$\left[(1-\phi_f) Y_{c_i} + \phi_f Y_{g_i}\right]_{0^-} = \left[(1-\phi_g) Y_{c_i} + \phi_g \left(1 + \frac{V_{g_i}}{u_g}\right) Y_{g_i}\right]_{0^+} \tag{30}$$

A summation of the above equations for all the condensed species GAP$_{(l)}$, GAP*$_{(l)}$, and C$_{(s)}$ gives

$$\left[(1-\phi_f)(1-Y_{RDX_c})\right]_{0^-} = \left[(1-\phi_g)\right]_{0^+} \tag{31}$$

Equations (28-31) are sufficient to solve the set of unknowns $(u, T, Y_i, \phi)$ at the propellant surface and provide the boundary conditions for the foam layer and gas phase.

The boundary conditions at the interface (melt front) between the solid phase and foam layer are

$$T_c = T_f = T_{\mathrm{melt}} \text{ and } \phi_f = 0 \quad \text{at } x = x_{\mathrm{melt}} \tag{32}$$

$$\left[\lambda_c \frac{dT_c}{dx} + \rho_c u_c Y_{\text{HMX}} h_{\text{HMX}_{s\to l}}\right]_{x_{\text{melt}}^-} = \left[\lambda_f \frac{dT_f}{dx}\right]_{x_{\text{melt}}^+} \tag{33}$$

The far-field conditions for the gas phase require the gradients of flow properties to be zero at $x = \infty$.

$$\frac{\partial \rho}{\partial x} = \frac{\partial u}{\partial x} = \frac{\partial Y_i}{\partial x} = \frac{\partial T}{\partial x} = 0 \text{ at } x = \infty \tag{34}$$

The condition at the cold boundary for the condensed phase ($x = -\infty$) is

$$T_c = T_i \quad \text{as } x \to -\infty \tag{35}$$

where $T_i$ is the pre-conditioned temperature of the propellant. The initial mass fractions of HMX and GAP are also provided as input parameters.

## V. NUMERICAL METHOD

The theoretical formulation established in the current work requires a robust computational scheme due to the numerical stiffness caused by chemical reactions and transport processes. All the conservation equations and associated boundary conditions are coupled and solved by a double-iteration procedure which treats the propellant surface temperature $T_s$ and burning rate $r_b$ as eigenvalues. The procedure continues with $T_s$ adjusted by an inner loop while $r_b$ is corrected by the outer iteration. The conservation equations for the subsurface region are solved first and the resulting species concentrations at the surface are used as the boundary conditions for the gas-phase region through the interfacial matching conditions. The next step involves integration of the gas-phase conservation equations to provide the temperature and species-concentration profiles. The non-equilibrium evaporation Equation (29) is then employed to check the convergence of $T_s$. If this is not successful, another inner iteration is repeated using an updated value of $T_s$. The outer iteration follows the same procedure as the inner loop, except that $r_b$ is used as the eigenvalue to check the interfacial energy continuity, Equation (28). Since only the burning rate and surface temperature, and not the interfacial species composition, are involved in the iterative procedure, the present algorithm performs quite well and significantly reduces the computational burden.

The conservation Equations (4-7) for the subsurface region are fully coupled. They are, however, solved by an uncoupled-iteration method. The method starts with an estimated temperature profile obtained by solving an inert energy equation, and then the conservation equations of mass and species concentrations are integrated using a fourth-order Runge-Kutta method. Equation (7) is subsequently solved with the newly obtained void fraction and species concentrations to obtain another temperature profile. Since the equations are solved separately, iteration is required to ensure a converged solution that satisfies all the conservation laws and boundary conditions.

The governing Equations (12-15) for the gas phase are fully coupled, but solved by an uncoupled-iteration method similar to the subsurface-region solver. Equation (13) is first solved using a fourth-order Runge-Kutta method to get the void fraction and the mass fractions of condensed species. Equations (12,14,15) are then solved using the Chemkin-Premix[83] package with some modifications since the governing equations have been changed to account for a two-phase system. The grid systems of the two solvers are different and direct interpolation is used to match the grid information.

## VI. DISCUSSION OF MODEL RESULTS

In the past decade, a significant amount of effort has been spent for modeling and simulating steady-state combustion of nitramine monopropellants[32,33], laser-induced ignition of RDX[39,40], and steady-state combustion of nitramine/GAP pseudo-propellants[37-39]. These models[32,33, 37-40] are based on the theoretical formulation and numerical method outlined in this chapter. Various important burning and ignition characteristics were investigated over a broad range of operating conditions. The roles of the subsurface multi-phase region in the propellant deflagration and ignition processes have been investigated by simulating complete combustion wave structures using the detailed reaction mechanism and updated thermophysical properties.

## *A. Steady-State Combustion of Nitramine Propellants*

Predicted temperature profiles of self-sustained RDX combustion over a pressure range from 1 to 90 atm[33] are shown in Figure 6. The temperature increases monotonically from its initial value of 293K, and levels off at a value close to the prediction by the chemical equilibrium analysis. The final flame temperature increases with increasing pressure, whereas the flame-standoff distance exhibits an opposite trend owing to enhanced chemical-reaction rates at high pressures. No evidence is obtained of the existence of a temperature plateau in the dark zone regardless of pressure, which is consistent with the experimental observations of self-sustained combustion of RDX monopropellant[36]. However, a dark-zone temperature plateau (at $T \sim 1500$ K) was present in the laser-assisted combustion of RDX, while the existence of the dark zone was not evident in the self-assisted combustion. Liau and Yang[36] indicated that the chemical preparation and fluid transport times of the intermediate species produced in the primary flame must be comparable in order to form a dark zone.

Figure 7 shows the burning rate as a function of pressure. Good agreement between predictions and measurements is obtained. A power law of the burning rate as a function of pressure is observed,

$$r_b = a\, p^n \tag{36}$$

where the pressure exponent $n$ is about 0.83 (with $p$ in atm), and the pre-exponential factor $a$ equals to 0.3 cm/s for $T_i = 293$K. The increased burning rate with pressure is attributed mainly to fast gas-phase exothermic reactions at high pressures and their influence on heat transfer to the condensed phase.

The temperature sensitivity of burning rate defined in Equation (37) is also examined.

$$\sigma_p = \left[ \frac{(\partial r_b)/r_b}{\partial T_i} \right]_p = \left[ \frac{\partial(\ln r_b)}{\partial T_i} \right]_p \tag{37}$$

The temperature sensitivity $\sigma_p$ stays around $0.0028\ K^{-1}$ for most cases. At elevated pressures, the heat feedback from the gas phase to the condensed phase is higher, and thus the effect of initial temperature on the interfacial energy balance becomes less important. A numerical analysis on the temperature sensitivity for low-pressure conditions was further performed by Beckstead and co-workers[34]. The predicted temperature sensitivity was determined to be too low compared to the measurements, mostly due to the uncertainties associated with the treatment of the condensed phase in the model.

The calculated species-concentration profiles were validated against experimental data[22], which was obtained by means of a time-of-flight mass spectrometry technique at 0.5 atm, as shown in Figure 8. Good agreement was obtained except for the region next to the surface. The discrepancy may arise from the ambiguity in determining the location of the propellant surface in experiments. Due to the limitation of the spatial resolution (500 μm), the diagnostic work defined the surface as the location where RDX was completely consumed. This analysis, however, predicted that an appreciable amount of RDX still existed at the surface since only limited RDX decomposition occurred in the subsurface region. If the spatial distribution of the calculated data was artificially shifted upward to the location where NO and HCN attained their peak values, then an improved agreement between the prediction and the measurement could be achieved. The species-concentration profiles revealed that the overall reaction mechanisms globally consist of three steps: (1) decomposition of RDX to $CH_2O$, HCN, $NO_2$, *etc.* near the surface, (2) first-stage oxidization which includes formation of NO and $H_2O$ as well as removal of $NO_2$, and (3) second-stage oxidization which includes conversion of HCN and NO to the final products such as CO, $N_2$, and $H_2$. It is worth noting that the highly exothermic reductions of HCN and NO usually occur at elevated temperature ($T \sim 2000$ K) owing to the large activation energies required to initiate these reactions, which provide the major heat source for raising the flame temperature to its final adiabatic value. The calculated molar fractions of the final product species are quite consistent with the chemical-equilibrium predictions, with the deviation being less than 2%.

The combustion wave structure at 100 atm was also predicted[33] and showed a close similarity to that at 1 atm except for the shorter flame-standoff distance (6 vs. 600 μm) and molten-layer thickness (2.1 vs. 66 μm). The major difference lies in a smaller void fraction. The shorter molten-layer thickness and higher burning rate yield a shorter residence time for condensed-phase reaction. Also, high pressure tends to retard the RDX evaporation, which dominates the gasification process in the two-phase layer. As evidenced by the large ratio of HCN to $CH_2O$ mole fraction, the endothermic decomposition, (R2), appears more profound at high-pressure conditions. This can be attributed to the higher surface temperature and heat transfer into the condensed phase.

A similar modeling approach was applied to study the combustion characteristics of HMX monopropellant. In this chapter, the model results pertaining to the combustion-wave structure of RDX monopropellant are focused. A comprehensive description of theoretical formulation and results for combustion of HMX monopropellant can be found in References 37 and 39.

### *B. Laser-Induced Ignition of RDX Monopropellant*

By extending the state-state model to include the transient behavior, the entire laser-induced ignition process of RDX in an argon environment has also been studied[39,40]. Figure 9 shows the predicted temporal evolution of the temperature field at an incident laser heat flux of 400 W/cm$^2$ under atmospheric pressure. The initial temperature is 300 K. The interface between the subsurface and gas-phase regions is set to be $x = 0$, with negative and positive values of the $x$-coordinate representing the subsurface and gas phase, respectively. The surface temperature is rapidly increased to 475 K within 1 ms, due to the high intensity of laser heat flux. The profiles for $t < 1$ ms represent inert heating of the thin surface layer with conductive heat losses to both the solid- and gas-phase regions. The temperature rises in the gas phase at $t = 2$ ms are primarily caused by radiant energy absorption rather than exothermic reactions, because the extent of RDX decomposition in the gas phase is very limited at this stage of the event. At $t = 2.9$ ms, exothermic gas-phase reactions start to occur, and a flame appears near the propellant surface at $t = 3$ ms. During the time period between 3 and 6 ms, the temperature continues to increase to around 1500 K, as a consequence of the heat release by exothermic reactions. As time further elapses, a luminous flame appears, and the temperature rises to its adiabatic temperature. The luminous flame is not stationary but regresses toward the surface. There is a time lag (about 4 ms) between the first appearances of the primary and secondary flames.

Figure 10 shows a close-up view of the temperature evolution in the condensed phase near the propellant surface. The transient development of thermal-wave penetration into the subsurface region is clearly observed. The characteristic thickness of the thermal layer in the subsurface region is much thinner than that in the gas-phase region. Phase transition from solid to liquid can be indicated by the distinct change of temperature gradient at $T_m = 478$ K. Since most of the $CO_2$ laser heat flux is absorbed by the thin surface layer due to the high absorption coefficient (2800 cm$^{-1}$) of RDX at the wavelength of 10.6 μm, the formation of the mushy zone can be safely ignored. However, some propellants, including RDX, are quite transparent to plasma irradiation in the UV/visible wavelength range; thus, the appearance of the mushy zone may be evident in that situation. Figure 11 shows the distributions of void fraction and species concentrations in the subsurface two-phase region when ignition is achieved at *t* = 7 ms. The extent of RDX decomposition in the condensed phase is very limited during the laser-induced ignition process up to 7 ms over the range of conditions studied, due to the short residence time and low temperature conditions. The molten layer in the subsurface region is not fully established within this time frame under atmospheric pressure. As indicated in the previous subsection, the steady-state combustion model predicts that the gas bubbles occupy about 45% of the volume at the surface under atmospheric pressure during self-sustained RDX combustion as a result of RDX evaporation and decomposition[33]. However, the surface void fraction during the self-sustained RDX combustion decreases significantly with increasing pressure[33].

The overall gaseous RDX ignition process can be divided into five distinct stages: thermal decomposition, first oxidation, chemical preparation, second oxidation, and completion stages. In stage I, RDX decomposes to low-molecular weight species, such as $CH_2O$, $N_2O$, $NO_2$, HCN, and HONO. This decomposition process is slightly endo-/exo-thermic or thermally neutral depending on the initial temperature. In stage II, oxidation reactions occur and release a significant amount of energy with the temperature reaching about 1500 K. The heat release in stage II is mainly caused by the conversion of $CH_2O$ and $NO_2$ to $H_2O$, NO, and CO, and to a lesser extent by the reactions of HCN and HONO. Stage III represents the chemical preparation time before the second oxidation reactions (stage IV) take place. The species formed in stage II are relatively stable, due to the high activation energies of their associated reactions, and require a finite time to oxidize further. The reduction of HCN and NO to $N_2$, CO, $H_2O$, and $H_2$ is largely responsible for the heat release in stage IV. Finally, all the final products are formed; no further reactions occur in stage V.

A parametric study for investigating the effect of the absorption coefficient of vapor RDX on the overall ignition process has been performed by varying the absorption coefficient by 15 %. The gas-phase temperature is rapidly increased by more than 300 K at t = 2 ms, with a small amount of the laser energy absorbed by the gas phase. At t = 2.9 ms, the gas-phase temperature rises to more than 800 K, caused by the heat release from the exothermic decomposition reactions in the gas phase. After the inert heating, the heat release from the exothermic reactions becomes much more pronounced than the laser energy absorbed by the gas phase. Since only a small amount of the laser energy was absorbed by the gas phase, a change by 15 % in absorption coefficient did not influence the inert heating time significantly. Overall, the effect of the absorption coefficient of vapor RDX on the $CO_2$ laser-induced ignition was not noticeable over the parameter range studied herein.

Figure 12 shows the calculated and measured ignition delays of RDX induced by $CO_2$ laser under atmospheric pressure. Excellent agreement is achieved between the predicted and experimental data for laser intensities less than 200 W/cm$^2$. For 400 W/cm$^2$, the predicted ignition delay matches the measurements by Parr *et al.*[23] and Lee *et al.*[84]. However, the measured data of Vilyunov and Zarko[50] do not agree with the model prediction for laser intensities above 200 W/cm$^2$. Vilyunov and Zarko showed that the ignition delay increases with increasing laser intensity above 200 W/cm$^2$, whereas the results of the current model as well as Parr *et al.*[23] and Lee *et al.*[84] revealed the opposite trend. Vilyunov and Zarko[50] stated that the RDX ignition was controlled by the solid-phase kinetics at low laser intensities (below 200 W/cm$^2$), whereas the gas-phase kinetics along with the liquid-phase decomposition governed the ignition process at high laser intensities. The current model, however, predicted that the gas-phase chemistry controlled the ignition process over the laser intensity range studied. Thus, the ignition delay became shorter at higher laser intensities, because the gasification rate at the propellant surface increased with increasing laser intensity. Vilyunov and Zarko[50] performed their experiment in both nitrogen and air under atmospheric pressure and found that the ignition delays were about the same within the measurement accuracy. Lee and Litzinger[84] used argon as an inert gas, whereas Parr and Hanson-Parr perform the experiment in air. The differences in ignition delay among these three sets of measured data, especially above 200 W/cm$^2$, may be caused by the variation in RDX sample preparation in each experiment. The RDX samples used by Parr and Hanson-Parr[23] and Lee and Litzinger[84] were pressed military-grade RDX. Information about the samples used by Vilyunov and Zarko[50] was not available.

In the experiment by Parr and Hanson-Parr[23], a significant time lag was obtained between the first light and go/no-go times (about 85 ~ 100 ms). First light was defined as the time when the luminous flame was first detected, whereas go/no-go was the time when a stable flame was achieved without the laser-assisted heating. The model predictions for the first light and go-no-go times, however, were about the same. In the experiments[23], the luminous flame progressed toward the surface immediately after the first light and moved away from the surface after the maximum temperature gradient was achieved near the surface. The model, however, did not predict this type of flame movement. The luminous flame continuously progressed toward the surface until steady-state deflagration was achieved. The discrepancy between model predictions and experimental observations may be attributed to the heat loss to the ambience. The entire ignition process was treated as adiabatic in the model, whereas heat losses from both the gas-phase flame and the condensed-phase region to the surrounding might be significant in the experiments, in which continuous laser heating was required in order to achieve self-sustained combustion by fully establishing the condensed flame. This suggests that during the ignition stage, heat loss in the condensed phase was too rapid compared to the heat transfer from the gas-phase flame to the surface.

The discrepancies among the existing experimental results may be attributed to the uncertainties associated with measurements under different types of experimental conditions. It is clearly evident that more measured data is needed for model validation. Nonetheless, the present model provides detailed insight into the key physiochemical processes involved in the laser-induced ignition of RDX, and can be effectively used to estimate ignition delay, heat release mechanisms, and flame structure.

## *C. Steady-State Combustion of HMX/GAP and RDX/GAP Pseudo-Propellants*

Recently, Yang and co-workers performed numerical analyses to investigate the combustion characteristics of HMX/GAP and RDX/GAP pseudo-propellants over a broad range of pressure and laser intensity with various compositions.[37-39] Summaries of the model results for both HMX/GAP and RDX/GAP are given below.

### 1. HMX/GAP Pseudo-Propellant

Figure 13 shows the temperature and species-concentration profiles in the gas phase during HMX/GAP pseudo-propellant combustion at a $CO_2$ laser intensity of 100 $W/cm^2$ under atmospheric pressure. The ratio of HMX to GAP mass fraction is 8:2. Reasonable agreement was achieved with the experimental data reported in Reference 3. The temperature rises rapidly from 677 K at the surface, levels off around 1200-1600 K, and further increases to its final value at 2780 K. The flame can be divided into three regions: 1.) the primary flame, 2.) the dark zone, and 3.) the secondary flame. The dark zone is a nonluminous region between the primary and the secondary flame, and is characterized with a temperature plateau. The concentrations of HCN, NO, and $H_2O$ in the dark zone appeared to be similar to those of pure nitramine propellants[3]. The rapid conversion of HCN and NO to $N_2$ and CO in the secondary flame zone were successfully predicted. These reactions are highly exothermic and usually take place at high temperatures due to their large activation energies. The predicted flame stand-off distance of 3 mm is slightly shorter than the measured value of 4 mm, partly because of the ambiguity in defining the propellant surface during experiments.

Figure 14 shows a close-up view of the primary flame immediately above the propellant surface, which extends over a length of 100 μm. The dominant reactions in this oxidation stage are R1-R3. The prediction of $N_2O$ concentration was satisfactory compared with the measurement[3]; however, $NO_2$ and $CH_2O$ appear to be consumed too fast. Intermediate reactions forming $CH_2O$ and $NO_2$ are still lacking in the near-surface region in order to yield better agreement with experimental results. Conversion of GAP and GAP$^*$ to $N_2$, HCN, CO, $NH_3$, $CH_2O$, $CH_3CHO$, $H_2O$, $C_2H_3CHO$, $C_2H_4$, $CH_3CHNH$, and $CH_2CHCHNH$ occurs in a very short distance (~10 μm). The GAP decomposition is a highly exothermic process releasing a significant amount of energy in the gas phase. However, at the same time, the heat feedback from the gas phase to the surface is reduced due to the dilution of reactive species by the GAP pyrolysis gases. The decomposed fuel fragments, such as $CH_2CHO$, $C_2H_3CHO$, $CH_3CHNH$, and $CH_2CHCHNH$, further react to form $CH_3$, HCO, $C_2H_3$, and $H_2CN$.

The species-concentration and temperature profiles in the foam layer are shown in Figure 15. An appreciable amount of HMX evaporates to form gas bubbles in this region, but the extent of decomposition through the pathways (R1) and (R2) appears to be limited. On the other hand, most of the GAP compound is consumed to become GAP* and $N_2$, releasing heat to support pyrolysis in the condensed phase. Further decomposition of GAP* according to (R4), however, is constrained due to the low temperature condition. The predicted surface temperature and foam-layer thickness are 677 K and 30 μm, respectively.

Figure 16 presents the corresponding temperature sensitivity of burning rate, which appears to be independent of pressure and has a value twice greater than that of pure HMX. In general, the effect of preconditioned temperature on propellant burning rate diminishes with increasing pressure and impressed laser intensity. The enhanced heat transfer to the propellant surface due to large energy release and reduced flame standoff distance in the gas phase at elevated pressure overrides the influence of preconditioned temperature in determining the energy balance at the surface, and consequently decreases the temperature sensitivity of burning rate.

Figure 17 shows the effect of propellant composition on burning rate at various pressures. The burning rate in general decreases with the addition of GAP, which releases a substantial amount of $N_2$ through the C-$N_3$ bond breaking in the near-surface region. Although the process is exothermic, the pressure of $N_2$ and large fuel fragments dilute the concentrations of surface reactive species, and consequently reduces the rate of energy release from HMX reactions. The heat feedback to the surface decreases accordingly, rendering a lower burning rate. Another factor contributing to this phenomenon is the blowing effect of the GAP compound, which tends to push the primary flame away from the surface. The situation is, however, different at high pressures. The burning rate of HMX/GAP pseudo-propellant with a mass ratio of 9:1 is greater than that of pure HMX for $p > 30$ atm.

The effect of laser intensity on burning rate for several mixture ratios at 10 and 100 atm, respectively. At 10 atm, the burning rate increases with increasing $CO_2$ laser intensity. Although GAP decomposition is highly exothermic, the burning rate decreases with increasing GAP concentration because the fuel-rich pyrolysis products of GAP reduce the flame temperature and move the flame away from the surface. At a high pressure of 100 atm, the intensive heat transfer from the flame to the surface overrides the effect of surface radiant energy absorption. The burning rate thus appears to be insensitive to the impressed laser intensity. The influence of GAP concentration on burning rate exhibits a different trend from that at 10 atm due to the variation of surface temperature, a phenomenon that has been elaborated in connection with the discussion of Figure 17.

The effects of laser heat flux and pressure on the burning rate of HMX/GAP pseudo-propellant (mass ratio 8:2) have also been studied. The impressed laser flux causes a substantial increase in burning rate at low pressures (*e.g.*, 1 and 10 atm). The effect, however, diminishes at high pressure, since the heat feedback from the gas phase overshadows the surface laser absorption in determining the energy balance at the surface. The heat transfer to the burning surface increases almost linearly with pressure. The melt-layer thickness and surface void fraction decrease with increasing radiant heat flux at low pressure, but remain almost fixed at high pressure. It should be noted that the bubble formation rate can be enhanced with increasing temperature, but may also be reduced by the decreased residence time resulting from the increased burning rate at high temperature. The present case shows a net decrease in the surface void fraction with increasing pressure.

### 2. RDX/GAP Pseudo-Propellant

The flame structure observed in experiments using TQMS[3] was reasonably well predicted by the model. Figure 18 shows the predicted and measured[3] species concentration profiles in the gas phase at 1 atm and 100 W/cm$^2$. Similar to the HMX/GAP combustion, it is found that HCN, NO, and $H_2O$ are the major intermediate products in the dark zone. The conversion of HCN and NO to $N_2$ and CO dominates the luminous flame while the consumption of formaldehyde, $NO_2$, and $N_2O$ accounts for the primary flame above the surface. In contrast to RDX combustion, a noticeable amount (1-2%) of $CH_3CHO$ was observed near the surface. Here, the agreements between the predicted and measured concentration profiles of CO, $CO_2$, and formaldehyde are not as good as the others. Chemical equilibrium calculation was also performed. This calculation result matches the model output but not the experimental data. Even though the agreement between measured and computed burning rates is reasonably good, further investigations into the combustion wave are suggested to resolve the discrepancy in flame structure.

In the foam layer, Figure 19 shows that the predicted temperature rises from the melt point of RDX at 478 K to around 590 K at the propellant surface. The mass fraction of liquid RDX originates at 0.8 and decreases slightly mostly through evaporation and partially through decomposition. The void fraction increases from 0 to almost 9 % due to the formation of bubbles containing vapor RDX and a small amount of decomposed gases. Consistent with the condensed-phase kinetics, the extent of GAP decomposition is negligible at temperatures lower than 600 K.

The mass fraction of GAP remains at 0.2 throughout the foam layer, and then evolves into the gas phase. Figure 20 shows the predicted temperature, void fraction, and condensed species concentration profiles in the region immediately above the propellant surface. GAP starts to decompose in the gas phase when the temperature reaches 700 K. At this stage, $GAP^*$ is immediately formed due to the elimination of $N_2$ and reaches its maximum concentration within a short distance (less than 0.004 cm). The peak value of $GAP^*$ mass fraction is less than 10%. The calculated concentration of carbon residue in this case is negligible. If the propellant surface is defined as the location where all condensed species are gasified, the surface temperature would be around 1000 K, consistent with GAP combustion.

Figure 21 shows the predicted pressure dependence of burning rate for a RDX/GAP pseudo-propellant with a mass ratio of 8:2. It is found that the burning rate-pressure relation follows a power law which is applicable to many propellants with the exponent $n = 1$, whereas $n = 0.83$ for pure RDX. The exponent value $n = 1$ indicates that the addition of GAP does alter the combustion characteristics of RDX. Figure 22 shows the temperature sensitivity defined in Equation (35) of burning rate at various pressures. The temperature sensitivity of burning rate decays at high pressures since the heat feedback is more profound than the effect of initial temperature on the burning rate.

Similar to results of the HMX/GAP analysis, the combustion characteristics of RDX/GAP pseudo-propellant at various pressures and initial temperatures were investigated[38]. The surface temperature increases linearly with increasing pressure on the logarithmic scale, but it is not very sensitive to the initial temperature. This is understandable because the surface temperature is resolved by an energy balance, and the heat flux is strongly dependant on the pressure but not the initial temperature. The adiabatic flame temperature increases with both increasing pressure and initial temperature. The increase is not linear due to the limitation of grid resolution and the non-linearity of chemical kinetics. The melt-layer thickness decreases with increasing pressure but is not sensitive to the initial temperature. In general, the melt-layer thickness decreases with increasing burning rate, but increases with the higher values of thermal conductivity of the propellant. As shown in Figure 21, the burning rate is linearly dependant on pressure, and thus the pressure dependence of melt-layer thickness is also linear. The initial temperature of propellant does not exhibit a strong effect on the melt-layer thickness, because both the burning rate and thermal conductivity are not very sensitive to the initial temperature. The surface void fraction decreases with increasing pressure, but increases with increasing initial temperature. It is not surprising because the bubble formation strongly depends on the evaporation process, which is retarded at high pressures but enhanced at high initial temperatures.

The effects of laser heat flux on the burning rate, surface heat flux, surface temperature, melt-layer thickness, and surface void fraction at pressure levels of 1, 10, and 100 atm were numerically investigated. The burning rate and surface temperature increase with increasing laser heat flux. The effect decays with increasing pressure because the heat feedback from the gas phase increases with increasing pressure. The melt-layer thickness exhibits an opposite trend; it decreases with increasing burning rate, and its decreasing rate is consistent with the increasing rate of burning rate. In contrast to the heat feedback from the gas phase at high pressures, the laser heat flux increases bubble formation, up to 50% at the surface at 1 atm and 300 W/cm$^2$.

The final set of results show the effects of binder mass fraction on combustion characteristics over a broad range of pressure and initial temperature. Here, it is possible to utilize the model to describe experimental observations. For example, the burning rate of pure GAP is higher than that of HMX, but the addition of GAP into HMX lowers the burning rate[24]. In contrast, recent measurements[3] show the enhancement of burning rate by adding GAP into RDX or HMX. Both observations have been reproduced by the model. Figure 23 shows the effects of initial composition and pressure on the burning rate of RDX/GAP pseudo propellants. The burning rate decreases in the case of higher GAP composition because GAP decomposition produces inert gases that dilute the concentrations of surface reactive species, and thus retard the heat feedback from the gas phase.

It is evident that the heat feedback is a controlling factor for the burning rate in all the cases without laser, because the pressure dependence of burning rate follows the same trend as that of heat feedback. The addition of GAP modifies the slopes (pressure dependencies) in Figure 23, but not in a consistent manner. A small amount of GAP (10% by weight) increases the slope and makes the system unstable, while more GAP (30% by weight) restores the slope to the pure RDX case but reduces the burning rate by more than 50%. Figure 24 shows the burning rates at 10 atm with various compositions and laser levels. The profiles of mass ratios 10:0 and 9:1 are very close, indicating the burning-rate change due to the addition of a small amount of GAP is negligible for laser heat fluxes ranging from 100 to 300 W/cm$^2$. For higher GAP compositions (20 and 30 % by weight), the burning rates decrease at 100 W/cm$^2$, but increase at 200 and 300 W/cm$^2$. The effect is more profound at low pressures since the conductive heat feedback from the gas phase is of less importance in the case of laser-assisted combustion. More experimental data, however, is required for model validation as well as an improved chemical kinetics mechanism of GAP decomposition.

## VII. CONCLUDING REMARKS

In the past decade significant progress has been made in modeling the steady-state combustion and transient ignition behavior of nitramine monopropellants and nitramine/GAP pseudo-propellants. The theoretical formulation is based on the conservation equations of mass, energy, and species for both the condensed and gas phases, and takes into account finite-rate chemical kinetics and variable thermophysical properties. These models have been applied to a broad range of operating conditions. Various important burning and ignition characteristics were investigated systematically, with emphasis placed on the detailed combustion-wave structure and the effect of the subsurface two-phase layer on propellant deflagration and ignition behavior. For pseudo-propellants, the effect of propellant composition on the burning rate at various pressures and heat fluxes was studied. In general, good agreement was achieved between the predicted and measured species-concentration and temperature profiles. Burning rates and their temperature and pressure sensitivities were reasonably predicted over a broad range of operating conditions. The complete ignition process from surface pyrolysis to steady-state combustion of RDX monopropellant was also investigated using the ignition model. Emphasis was placed on the ignition delay and key physiochemical processes responsible for achieving ignition. The predicted ignition delay shows good agreement with experimental data. In spite of the accomplishments achieved so far, several challenges remain. One major difficulty in both experimental and theoretical investigations lies in the treatment of the two-phase near-surface region, which includes an array of intricacies such as thermal decomposition, subsequent reactions, evaporation, bubble formation and interaction, and interfacial transport of mass and energy between the gas and condensed phases. The lack of reliable thermophysical properties poses another limitation in model accuracy. Nonetheless, the existing models provide a solid basis for investigating various underlying processes involved in the combustion and ignition of energetic materials.

# VIII. ACKNOWLEDGEMENTS

This work was supported partly by the Pennsylvania State University, partly by the Army Research Office under Contract DAAL 03-92-G-0118, and partly by the California Institute of Technology Multidisciplinary University Research Initiative under ONR Grant No. N00014-95-1-1338. The authors are indebted to Dr. Yeong Cherng (John) Liau for his contributions in developing the RDX ignition and combustion models.

# IX. REFERENCES

1. T.P. Parr and D.M. Hanson-Parr, in "Solid Propellant Chemistry, Combustion, and Motor Interior Ballistics", edited by V. Yang, T. B. Brill, and W. Z., Ren (Vol. 185, Progress in Astronautics and Aeronautics, AIAA, Reston, VA, 2000), p. 381.
2. O.P. Korobeinichev, in "Solid Propellant Chemistry, Combustion, and Motor Interior Ballistics", edited by V. Yang, T. B. Brill, and W. Z., Ren (Vol. 185, Progress in Astronautics and Aeronautics, AIAA, Reston, VA, 2000), p. 335.
3. T.A. Litzinger, Y.-J. Lee, and C.-J. Tang, in "Solid Propellant Chemistry, Combustion, and Motor Interior Ballistics", edited by V. Yang, T. B. Brill, and W. Z., Ren (Vol. 185, Progress in Astronautics and Aeronautics, AIAA, Reston, VA, 2000), p. 355.
4. D. Chakraboty, D. and M.C. Lin, in "Solid Propellant Chemistry, Combustion, and Motor Interior Ballistics", edited by V. Yang, T. B. Brill, and W. Z., Ren (Vol. 185, Progress in Astronautics and Aeronautics, AIAA, Reston, VA, 2000), p. 33.
5. T. B. Brill, M. C. Beckstead, J. E., Flanagan, M. C. Lin, T. A. Litzinger, R. H. W. Waesche, and C. A. Wight, *J. Prop. Power* **18,** 824 (2002).
6. B.C. Beard, Propellants, *Explosives, and Pyrotechnics* **16,** 81 (1991).
7. H.H. Krause, N. Eisenreich, and A. Pfeil, *Propellants, Explosives, and Pyrotechnics* **17**, 179 (1992).
8. R. Behrens, Jr. and S.N. Bulusu, *J. Phys. Chem*. **96**, 8877 (1992).
9. C.A. Wight and T.R. Botcher, *J. Amer. Chem. Soc*. **114**, 8303 (1992).
10. R.R. Botcher and C.A. Wight, *J. Phys. Chem*. **97**, 9149 (1993).
11. A. Zenin, *J. Prop. Power* **11**, 752 (1995).
12. T.B. Brill, *J. Prop. Power* **11**, 740 (1995).

13. E.S. Kim, H.S. Lee, C.F. Mallery, and S.T. Thynell, *Combust. Flame* **110**, 239 (1997).

14. T.A. Litzinger, B.L. Fetherolf, Y.-J. Lee, and C.-J. Tang, *J. Prop. Power* **11**, 698 (1995).

15. S.T. Thynell, P.E. Gongwer, and T.B. Brill, *J. Prop. Power* **12**, 933 (1996).

16. C.Y. Lin, H.I. Wang, M.C. Lin, and C.F. Williams, *Intern. J. Chem. Kinetics* **22**, 455 (1990).

17. D.M. Hanson-Parr and T.P. Parr, *J. Energetic Materials* **17**, 1 (1999).

18. R.A. Isbell and M.Q. Brewster, *Propellants, Explosives, and Pyrotechnics* **23**, 218 (1998).

19. T.B. Brill, *Prog. Energy Combust. Sci.* **18**, 91 (1992).

20. R.A. Isbell and M.Q.J. Brewster, *Thermophysics and Heat Transfer* **11**, 65 (1997).

21. A.I. Atwood, T.L. Boggs, P.O. Curran, T.P. Parr, and D.M. Hanson-Parr, *J. Prop. Power* **15**, 740 (1999).

22. O.P. Korobeinichev, L.V. Kuibida, V.N. Orlov, A.G. Tereshchenko, K.P. Kutsenogii, R.V. Mavliev, N.E. Ermolin, V.M. Fomin, and I.D. Emel'yanov, *Mass-Spektrom. Khim. Kinet*. 73 (1985).

23. T.P. Parr and D.M. Hanson-Parr, *Twenty-Seventh Symp. (International) on Combust*. 2301 (1998).

24. C.F. Melius, in "Chemistry and Physics of Energetic Materials" edited by S. Bulusu (Kluwer Academic , Norwell, MA, 1990), p. 21.

25. R.A. Yetter, F.L. Dryer, M.T. Allen, and J.L. Gatto, *J. Prop. Power* **11**, 666 (1995).

26. S.C. Li, F.A. Williams, and S.B. Margolis, *Combust. Flame* **80**, 329 (1990).

27. S.B. Margolis and F.A. Williams, *J. Prop. Power* **11**, 759 (1995).

28. S.C. Li and F.A. Williams, *J. Prop. Power* **12**, 302 (1996).

29. K. Prasad, R.A. Yetter, and M.D. Smooke, *Combust. Sci. Tech*. **124**, 35 (1997).

30. K. Prasad, M. Smooke, and R.A. Yetter, *Combust. Flame* **115**, 406 (1998).

31. M.S. Miller and W.R. Anderson, in “Solid Propellant Chemistry, Combustion, and Motor Interior Ballistics”, edited by V. Yang, T. B. Brill, and W. Z., Ren (Vol. 185, Progress in Astronautics and Aeronautics, AIAA, Reston, VA, 2000), p. 501.
32. Y.-C. Liau, The Pennsylvania State University, Department of Mechanical Engineering, Ph.D. Diss. (1996).
33. Y.-C. Liau, and V. Yang, *J. Prop. Power* **11**, 729 (1995).
34. J.E. Davidson and M.W. Beckstead, *J. Prop. Power* **13**, 375 (1997).
35. J.E. Davidson and M.W. Beckstead, *Twenty-Sixth Symp. (International) on Combust*. 1989 (1996).
36. Y.-C. Liau and V. Yang, *AIAA Paper 97-0589* (1997).
37. E.S. Kim, V. Yang, and Y.-C. Liau, *Combust. Flames* **131**, 227 (2002).
38. Y.-C Liau, V. Yang, and S.T. Thynell, in “Solid Propellant Chemistry, Combustion, and Motor Interior Ballistics”, edited by V. Yang, T. B. Brill, and W. Z., Ren (Vol. 185, Progress in Astronautics and Aeronautics, AIAA, Reston, VA, 2000), p. 477.
39. E.S. Kim, The Pennsylvania State University, Department of Mechanical Engineering, Ph.D. Diss. (2000).
40. Y.-C. Liau, E.S. Kim, and V. Yang, *Combust. Flames* **126**, 1680 (2001).
41. T.L. Boggs, in “Fundamentals of Solid Propellant Combustion”, edited by K.K. Kuo and M. Summerfield (Vol. 90, Progress in Astronautics and Aeronautics, 1984) p.121.
42. R.A. Fifer, in “Fundamentals of Solid Propellant Combustion”, edited by K.K. Kuo and M. Summerfield (Vol. 90, Progress in Astronautics and Aeronautics, 1984) p. 177.
43. M.H. Alexander, P.J. Dagdigian, M.E. Jocox, C.E. Kolb, C.F. Melius, H. Rabitz, M. Smooke, and W. Tsang, *Prog. in Energy Combust. Sci*. **17**, 263 (1991).

44. V. Yang, T.B. Brill, and W.Z. Ren, (Eds.), "Solid Propellant Chemistry, Combustion, and Motor Interior Ballistics" (Vol. 185, Progress in Astronautics and Aeronautics, AIAA, Reston, VA, 2000).
45. M. Benreuven, L.H. Caveny, R.J. Vichnevetsky, and M. Summerfield, *Sixteenth Symp. (International) on Combust.* 1223 (1976).
46. N.E. Ermolin, O.P. Korobeinichev, L.V. Kuibida, and V.M. Formin, *Fizika Goreniya I Vzryva*, Vol. 22, (1986) 54.
47. E.W. Price, H.H. Bradley, G.L. Dehority, and M.M. Ibiricu, *AIAA J.* **4**, 1153 (1966).
48. A.K. Kulkarni, M. Kumar, and K.K. Kuo, *AIAA J.* **20**, 243 (1982).
49. C.E. Hermance, in "Fundamentals of Solid Propellant Combustion", edited by K.K. Kuo and M. Summerfield (Vol. 90, Progress in Astronautics and Aeronautics, 1984) p. 239.
50. V.N. Vilyunov and V.E. Zarko, "Ignition of Solids" (Elsevier Science Publishers, NY, 1989).
51. L. Strakouskiy, A. Cohen, R. Fifer, R. Beyer, and B. Forch, "Laser Ignition of Propellants and Explosives" (ARL-TR-1699, Army Research Laboratory, Aberdeen Proving Ground, MD, 1998).
52. S.D. Baer and N.W. Ryan, *AIAA J.* **6**, 872 (1968).
53. H.H. Bradley, *Combust. Sci. Technol.* **2**, 11 (1970).
54. A. Linan, and F.A. Williams, *Combust. Sci. Technol.* **3**, 91 (1971).
55. A. Linan, and F.A. Williams, *Combust. Flame* **18**, 85 (1972).
56. F.A. Williams, *AIAA J.* **4**, 1354 (1966).
57. C.H. Waldman and M. Summerfield, *AIAA J.* **7**, 1359 (1969).
58. C.H. Waldman, *Combust. Sci. Technol.* **2**, 81 (1970).
59. H.H. Bradley and F.A. Williams, *Combust. Sci. Technol.* **2**, 41 (1970).
60. W.H. Andersen, *Combust. Sci. Technol.* **2**, 23 (1970).
61. W.H. Andersen, Combust. *Sci. Technol.* **5**, 43 (1972).

62. W.H. Andersen, Combust. *Sci. Technol*. **5**, 75 (1972).

63. A. Linan, and A. Crespo, *Combust. Sci. Technol*. **6**, 223 (1972).

64. T. Niioka, *Combust. Sci. Technol*. **18**, 207 (1978).

65. C.E. Hermance, R. Shinnar, and M. Summerfield, *Astronautica Acta* **12**, 95 (1966).

66. T. Kashiwagi, B.W. MacDonald, H. Isoda, and M. Summerfield, *Thirteenth Symp. (International) on Combust.*, 1073 (1971).

67. C.E. Hermance and R.K. Kumar, *AIAA J*. **8**, 1551 (1970).

68. R.K. Kumar and C.E. Hermance, *AIAA J*. **9**, 615 (1971).

69. R.K. Kumar and C.E. Hermance, *Combust. Sci. Technol*. **4**, 191 (1972).

70. R.K. Kumar and C.E. Hermance, Combust. *Sci. Technol*. **14**, 169 (1976).

71. M. Kindelan, and F.A. Williams, Combust. Sci. Technol. **16,** 47 (1977).

72. S. Ritchie, S. Thynell, and K.K Kuo, *J. Prop. Power* **13**, 367 (1997).

73. K. Puduppakkiam and M.W. Beckstead, *37th JANNAF Combust. Subcomm. Meeting*, (CPIA Publ., 2000).

74. C.-J. Tang, Y. Lee, and T. A. Litzinger, *Combust. Flame* **117**, 244 (1999).

75. H. Arisawa, and T. B. Brill, *Combust. Flame* **112**, 533 (1998).

76. N. Kubota and T. Sonobe, *Twenty-Third Symp. (International) on Combust.,*1331 (1990).

77. G. Lengellé, B. Fourest, J. C. Godon, and C. Guin, *AIAA Paper 93-2413* (1993).

78. J. E. Flanagan, D. O. Woolery, and R. L. Kistner, *AFAL-TR-87-107* (Air Force Astronautics Laboratory, Edwards AFB, CA, 1987).

79. M. Faber, S. P. Harris, and R. D. Srivastava, *Combust. Flame* **55**, 203 (1984).

80. A. A. Zenin, and S. V. Finjakov, *AIAA Paper 2000-1032* (2000).

81. G. S. Sysak, E. S. Kim, and S. T. Thynell, *35th JANNAF Combust. Subcomm. Meeting*, (CPIA Publ., 1998).

82. M. Frenklach, T. Bowman, G. Smith, and B. Gardiner, "GRI-MECH 1.2," http://euler.berkeley.edu/gri_mech/index.html.

83. R.J. Kee, J.F. Grcar, M.D. Smooke, and J.A. Miller, "A Fortran Program for Modeling Steady, Laminar, One-Dimensional" (Premixed Flames, Sandia Report SAND85-8240, Sandia National Laboratories, Albuquerque, NM, 1985).

84. Y.J. Lee and T.A. Litzinger, private communication, The Pennsylvania State University, University Park, PA, 1995.

# X. TABLES

## Table 1

## Subsurface Chemical Reactions and Rate Parameters

| No. | Reaction | $A^{a,c}$ | $E^{b,c}$ | Reference |
|---|---|---|---|---|
| R1 | $HMX_{(l)} \rightarrow 4CH_2O + 4N_2O$ | $5.81\times10^{10}$ | 34,000 | 34 |
| | | $1.00\times10^{13}$ | 34,400 | 12 |
| R2 | $HMX_{(l)} \rightarrow 4HCN + 2\ (NO_2 + NO + H_2O)$ | $1.66\times10^{14}$ | 44,100 | 34 |
| | | $1.00\times10^{16}$<br>.5 | 44,100 | 12 |
| R3 | $GAP56_{(l)} \rightarrow GAP56^{*}_{(l)} + 56N_2$ | $5\times10^{15}$ | 41,500 | 38 |
| R4 | $GAP56^{*}_{(l)} \rightarrow 25.6HCN + 15.8CO + 14.4NH_3 + 17.8CH_2O + 16CH_3CHO + H_2O + 6.4C_2H_3CHO + 1.5C_2H_4 + 8CH_3CHNH + 8CH_2CHCHNH + 14.6C_{(s)}$ | $1.28\times10^{19}$ | 53,000 | 38 |
| R5 | $HMX_{(l)} \Leftrightarrow HMX_{(g)}$ | See Reference 5 | - | 38 |
| R6 | $CH_2O + NO_2 \rightarrow CO + NO + H_2O$ | $802\times T^{2.77}$ | 13,730 | 16 |
| R7 | $CH_3CHO + M = CH_3 + HCO + M$ | $7\times10^{15}$ | 81,770 | 38 |
| R8 | $C_2H_3CHO + M = C_2H_3 + HCO + M$ | $10^{16}$ | 97,600 | 38 |
| R9 | $CH_3CHNH + M = CH_3 + H_2CN + M$ | $10^{16}$ | 63,700 | 38 |
| R10 | $CH_2CHCHNH + M = C_2H_3 + H_2CN + M$ | $10^{16}$ | 66,900 | 38 |

[a] A = pre-exponential factor [b] E = activation energy [c] Units are in mol, cm, s, K, and cal

# XI. FIGURE CAPTIONS

Figure 1. Molecular structures of RDX, HMX, and GAP.

Figure 2. Strand of RDX burning in a stagnant environment.

Figure 3. Schematic diagram showing various regions in RDX combustion-wave structure.

Figure 4. Physiochemical processes involved in laser-induced ignition of RDX.

Figure 5. Combustion-wave structure of HMX/GAP pseudo-propellant at 1 atm.

Figure 6. Temperature profiles of self-sustained RDX combustion at various pressures.

Figure 7. Effect of pressure on strand burning rate of RDX monopropellant; self-sustained combustion.

Figure 8. Distributions of major species concentrations of self-sustained combustion of RDX at 0.5 atm.

Figure 9. Evolution of temperature field during laser-induced ignition of RDX in argon at p = 1 atm and $\dot{Q}''_{\text{laser}} = 400$ W/cm$^2$.

Figure 10. Close-up view of temperature evolution in subsurface region during laser-induced ignition of RDX at p = 1 atm and $\dot{Q}''_{\text{laser}} = 400$ W/cm$^2$.

Figure 11. Close-up view of temperature and species-concentration profiles in subsurface region at t = 7 ms (p = 1 atm and $\dot{Q}''_{\text{laser}} = 400$ W/cm$^2$).

Figure 12. Effect of $CO_2$ laser intensity on ignition delay of RDX monopropellant.

Figure13. (a) Calculated and (b) measured[3] species-concentration profiles of gas-phase flame of HMX/GAP pseudo propellant (mass ratio 8:2) at 1 atm and laser intensity of 100 W/cm$^2$.

Figure 14. Temperature and species-concentration profiles in near-surface region of HMX/GAP pseudo propellant (mass ratio 8:2) combustion at 1 atm and laser intensity 100 W/cm$^2$.

Figure 15. Temperature and species-concentration profiles in subsurface of HMX/GAP pseudo propellant (mass ratio 8:2) combustion at 1 atm and laser intensity of 100 W/cm$^2$.

Figure 16. Temperature sensitivity of burning rate of HMX/GAP pseudo propellant (mass ratio 8:2); self-sustained combustion.

Figure 17. Effect of propellant composition on burning rate at various pressures; self-sustained combustion.

Figure 18. (a) Calculated and (b) measured[3] species profiles of the gas-phase flame of RDX/GAP pseudo propellant (mass ratio 8:2) at 1 atm and laser intensity 100 W/cm$^2$.

Figure 19. Predicted flame structure in the foam layer of RDX/GAP pseudo propellant (mass ratio 8:2) at 1 atm and laser intensity 100 W/cm$^2$.

Figure 20. Predicted temperature, void fraction, and condensed species concentration profiles in the near surface region of RDX/GAP pseudo propellant (mass ratio 8:2) at 1 atm and laser intensity 100 W/cm$^2$.

Figure 21. Predicted pressure dependence of burning rate of RDX/GAP pseudo propellant (mass ratio 8:2).

Figure 22. Predicted temperature sensitivity of burning rate of RDX/GAP pseudo propellant (mass ratio 8:2).

Figure 23. Predicted effect of propellant formulation on burning rate at various pressures.

Figure 24. Predicted effect of propellant formulation on burning rate at various laser and composition levels.

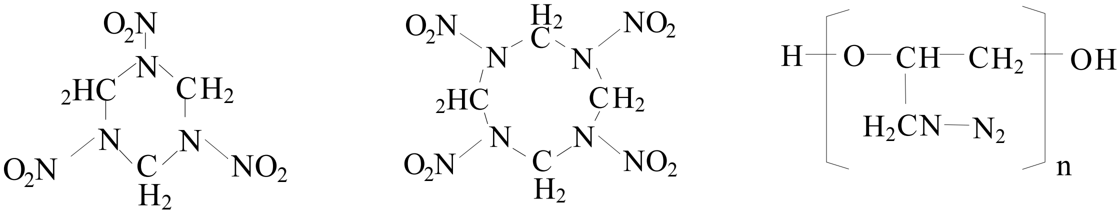

RDX HMX GAP

Figure 1. Molecular structures of RDX, HMX, and GAP.

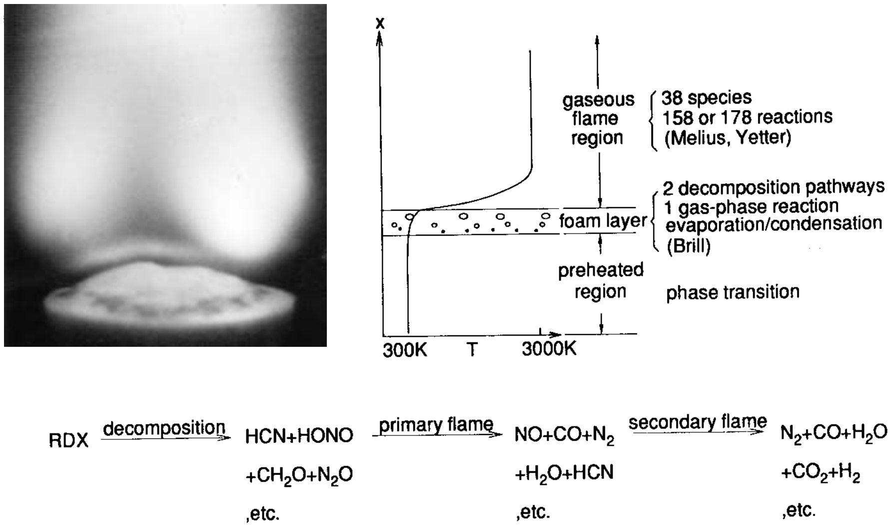

Figure 2. Strand of RDX burning in a stagnant environment.

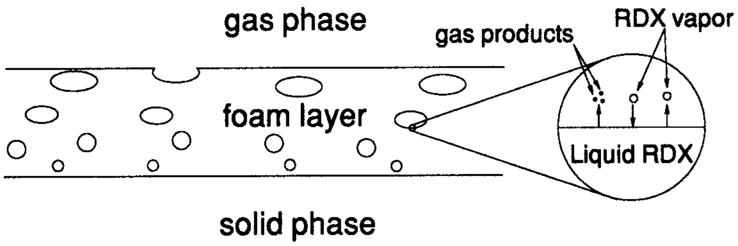

Figure 3. Schematic diagram showing various regions in RDX combustion-wave structure.

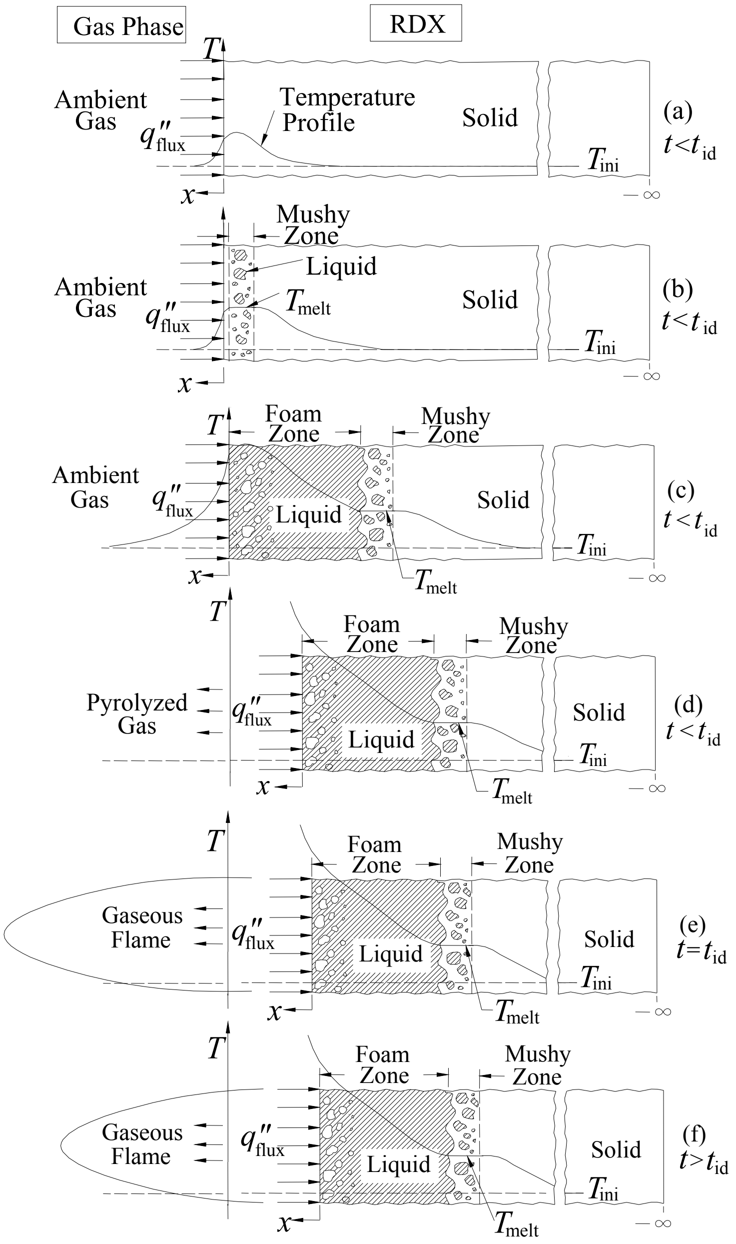

Figure 4. Physiochemical processes involved in laser-induced ignition of RDX.

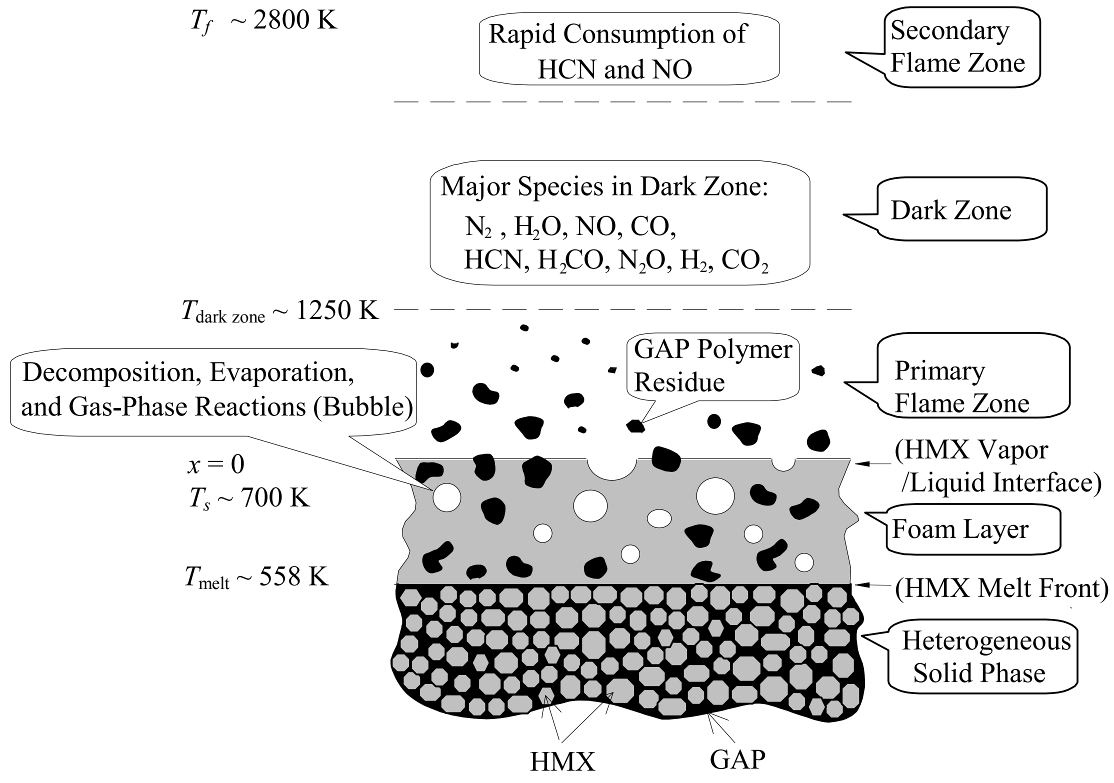

Figure 5. Combustion-wave structure of HMX/GAP pseudo-propellant at 1 atm.

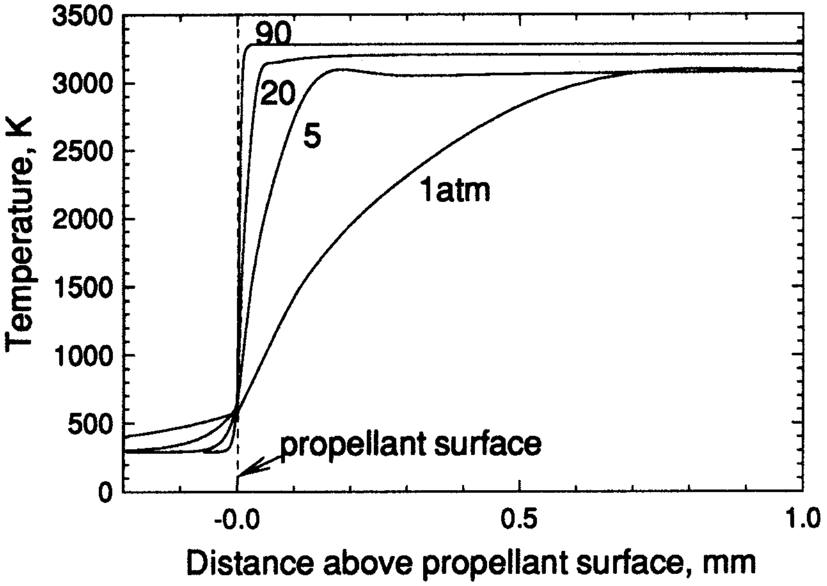

Figure 6. Temperature profiles of self-sustained RDX combustion at various pressures.

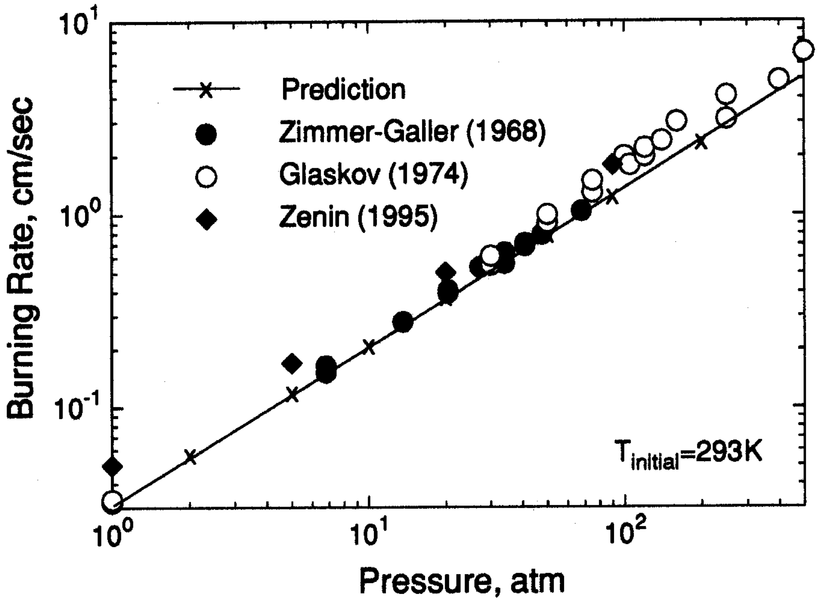

Figure 7. Effect of pressure on strand burning rate of RDX monopropellant; self-sustained combustion.

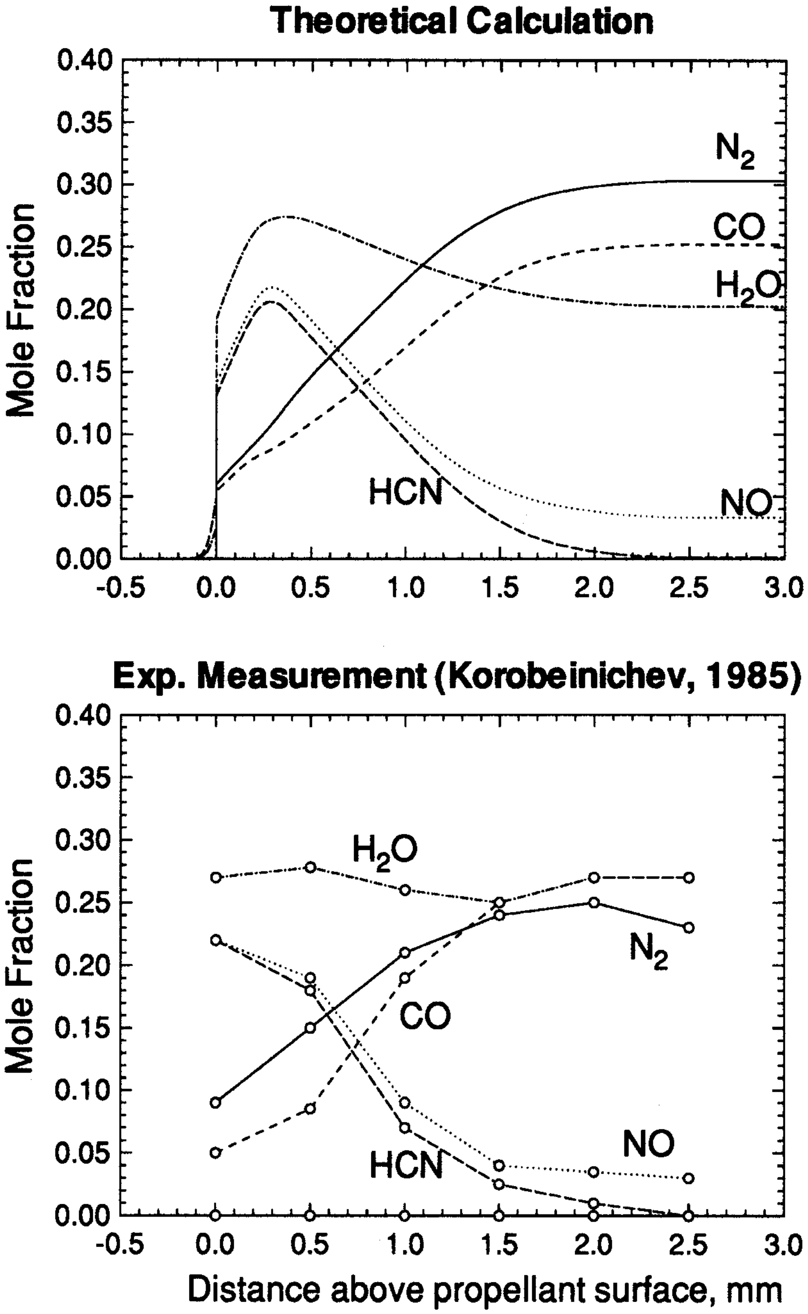

Figure 8. Distributions of major species concentrations of self-sustained combustion of RDX at 0.5 atm.

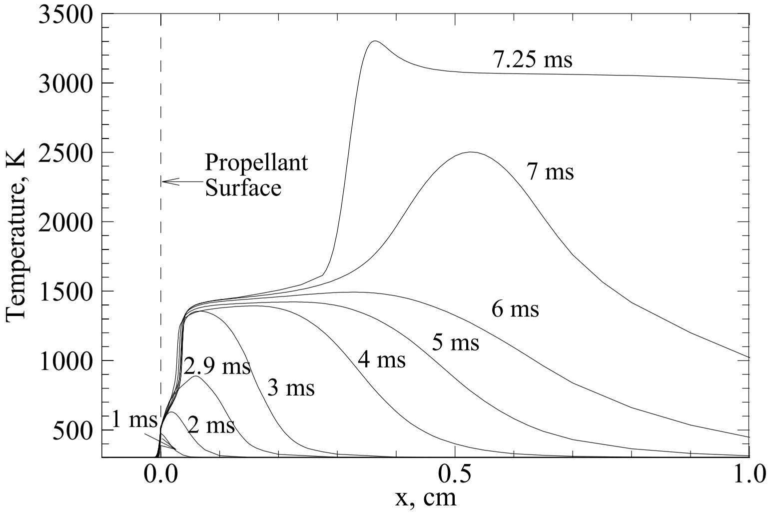

Figure 9. Evolution of temperature field during laser-induced ignition of RDX in argon at p = 1 atm and $\dot{Q}''_{\text{laser}} = 400$ W/cm$^2$.

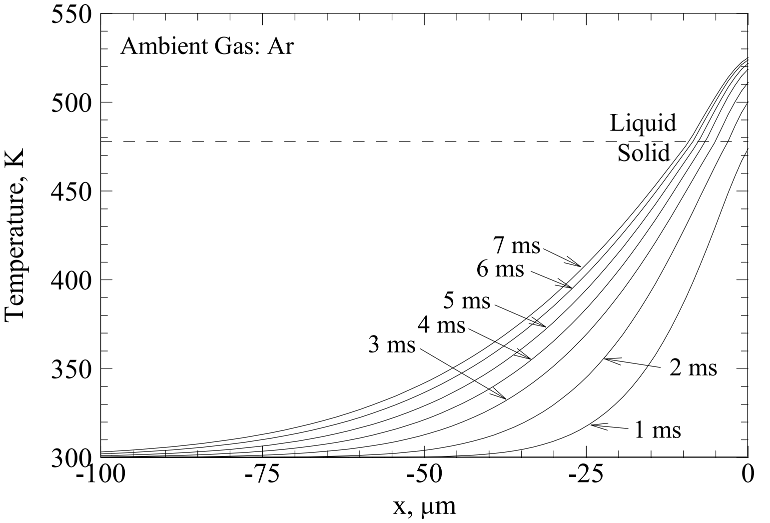

Figure 10. Close-up view of temperature evolution in subsurface region during laser-induced ignition of RDX at p = 1 atm and $\dot{Q}''_{\text{laser}} = 400$ W/cm$^2$.

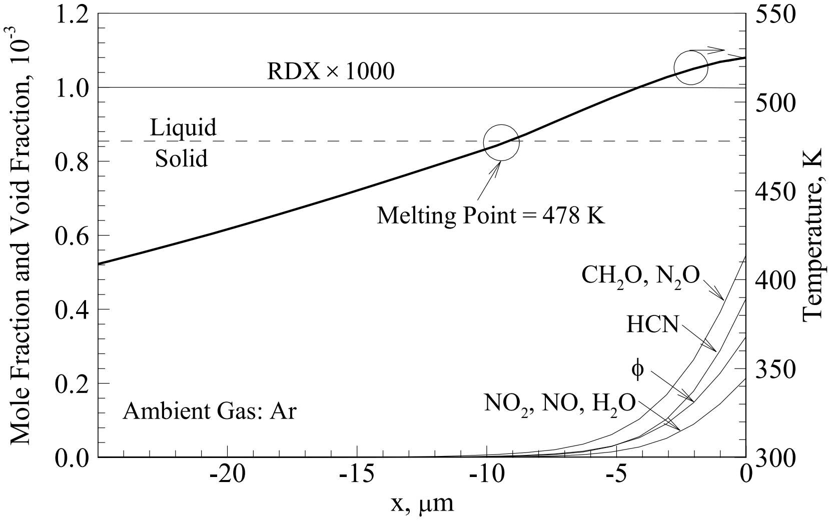

Figure 11. Close-up view of temperature and species-concentration profiles in subsurface region at t = 7 ms (p = 1 atm and $\dot{Q}''_{\text{laser}}$ = 400 W/cm$^2$).

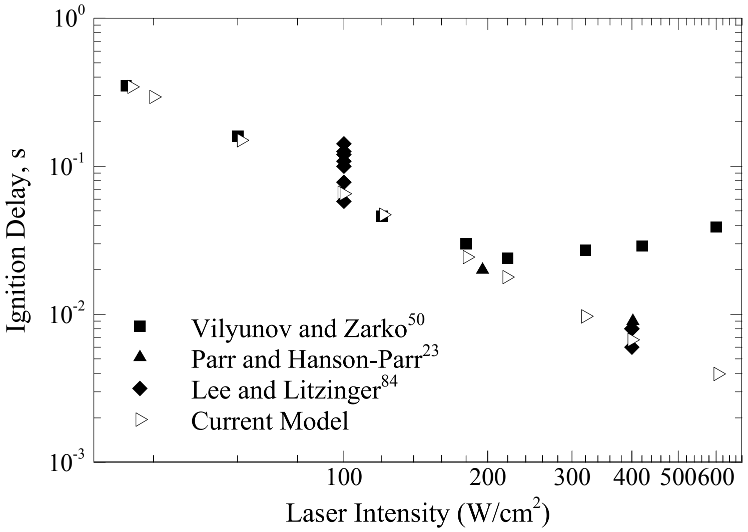

Figure 12. Effect of $CO_2$ laser intensity on ignition delay of RDX monopropellant.

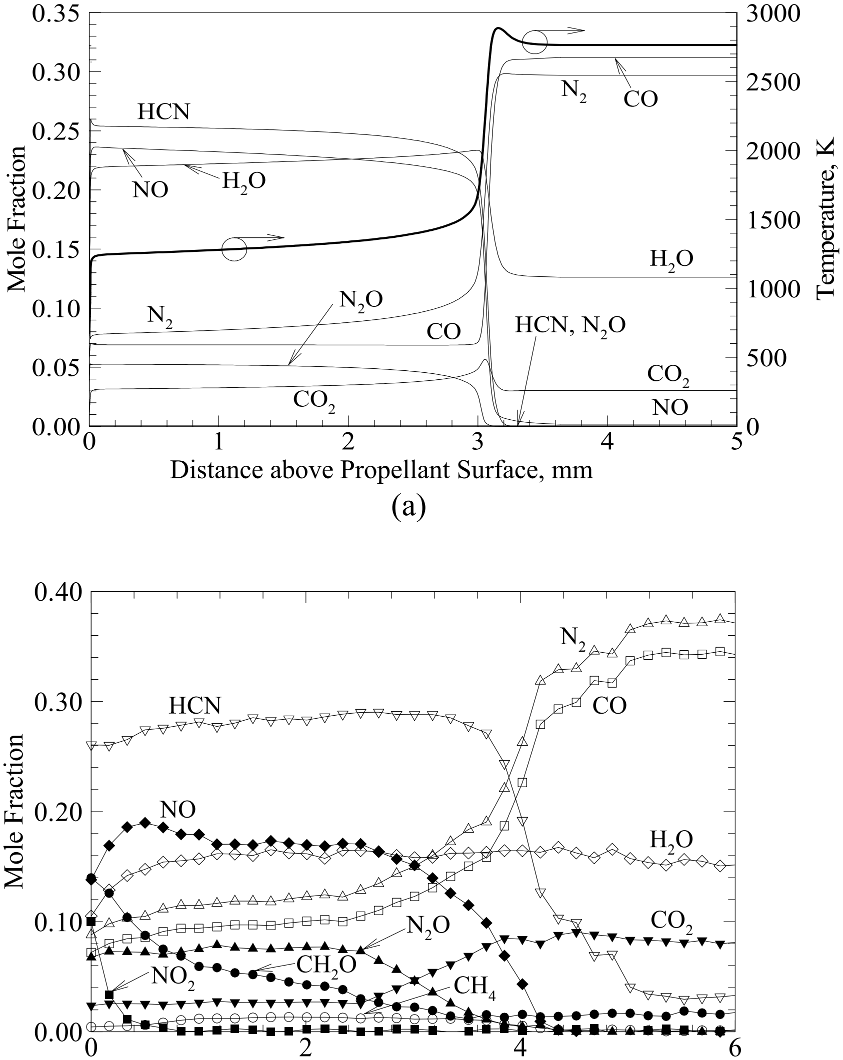

(a)

(b)

Figure 13. (a) Calculated and (b) measured[3] species-concentration profiles of gas-phase flame of HMX/GAP pseudo propellant (mass ratio 8:2) at 1 atm and laser intensity of 100 W/cm$^2$.

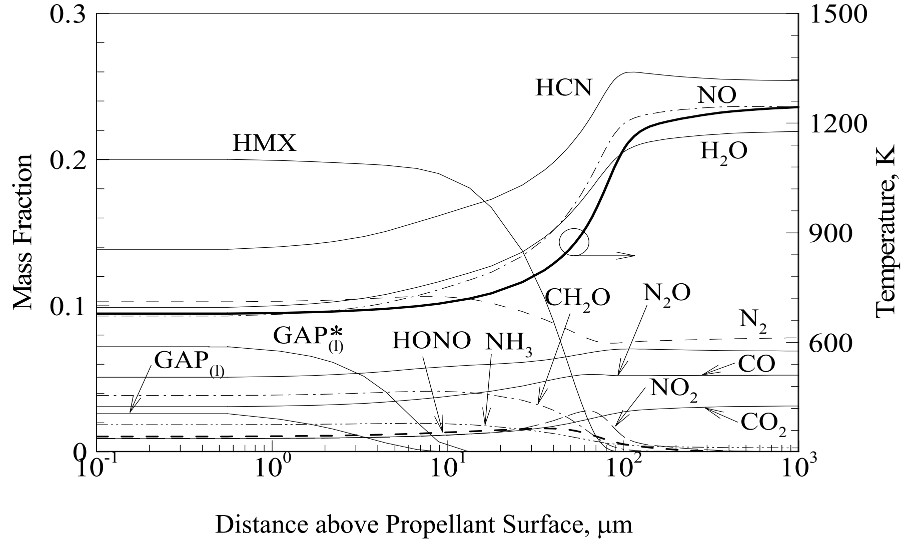

Figure 14. Temperature and species-concentration profiles in near-surface region of HMX/GAP pseudo propellant (mass ratio 8:2) combustion at 1 atm and laser intensity 100 W/cm$^2$.

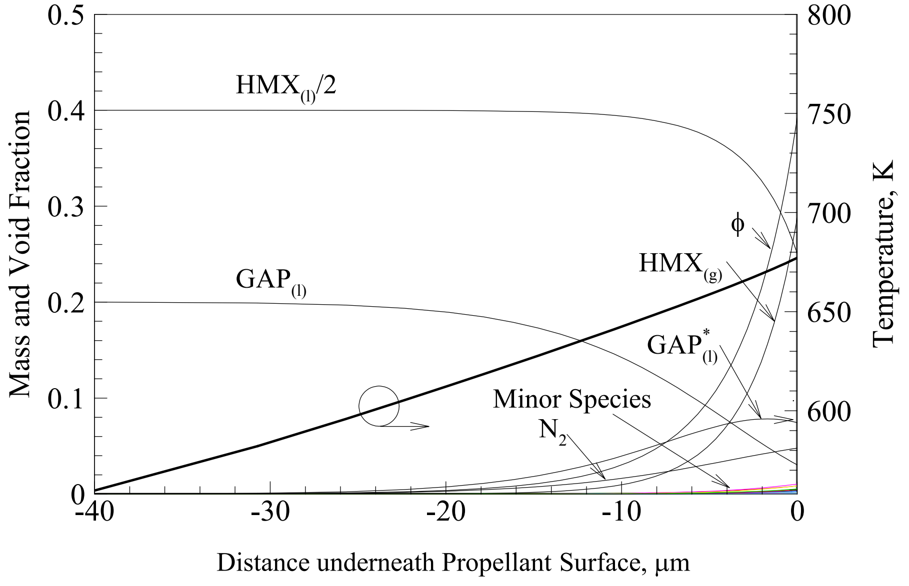

Figure 15. Temperature and species-concentration profiles in subsurface of HMX/GAP pseudo propellant (mass ratio 8:2) combustion at 1 atm and laser intensity of 100 W/cm$^2$.

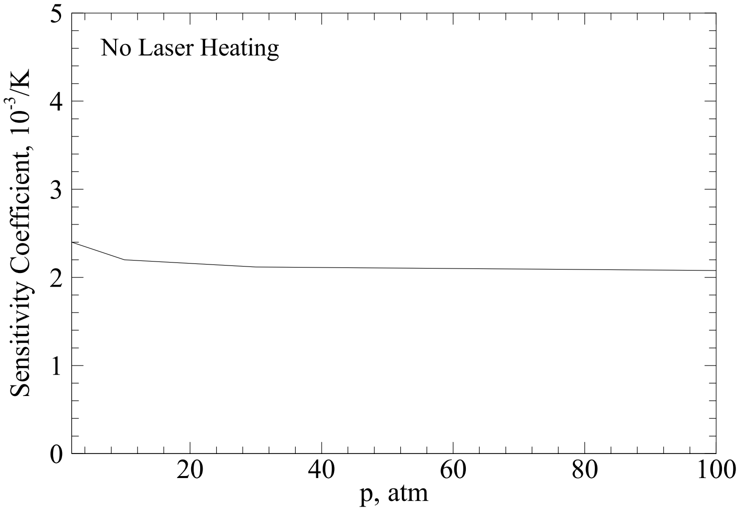

Figure 16. Temperature sensitivity of burning rate of HMX/GAP pseudo propellant (mass ratio 8:2); self-sustained combustion.

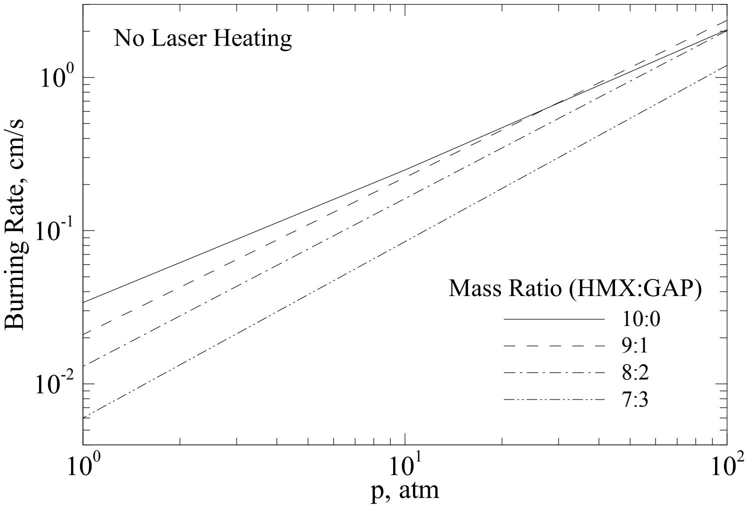

Figure 17. Effect of propellant composition on burning rate at various pressures; self-sustained combustion.

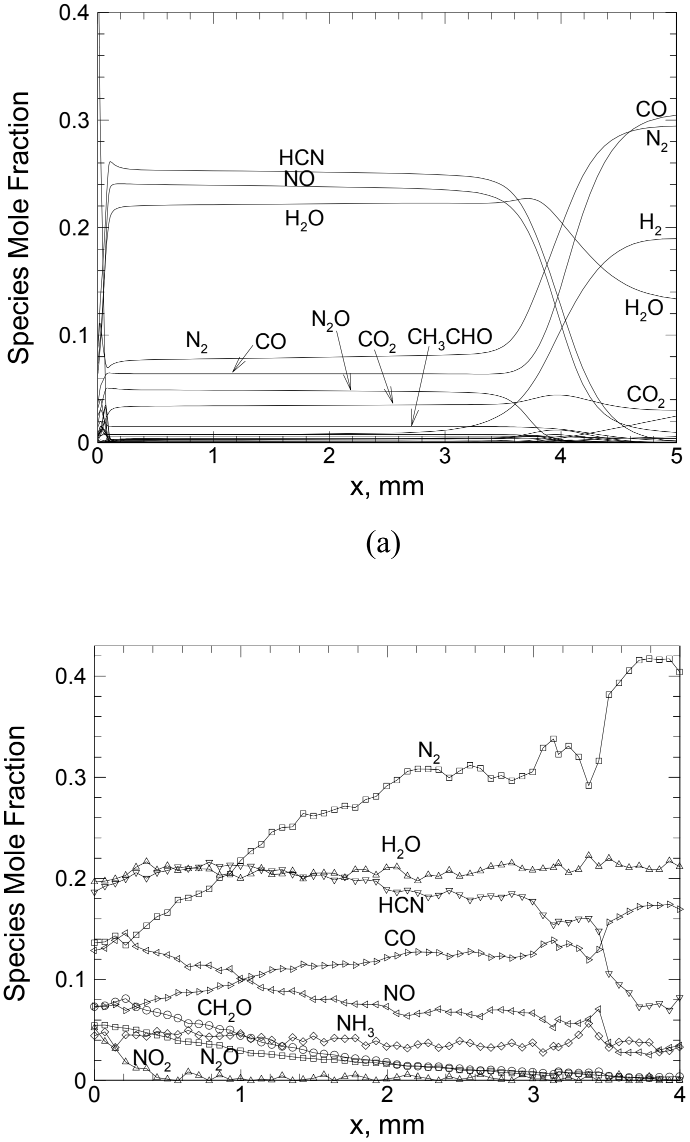

(a)

(b)

Figure 18. (a) Calculated and (b) measured[3] species profiles of the gas-phase flame of RDX/GAP pseudo propellant (mass ratio 8:2) at 1 atm and laser intensity 100 W/cm$^2$.

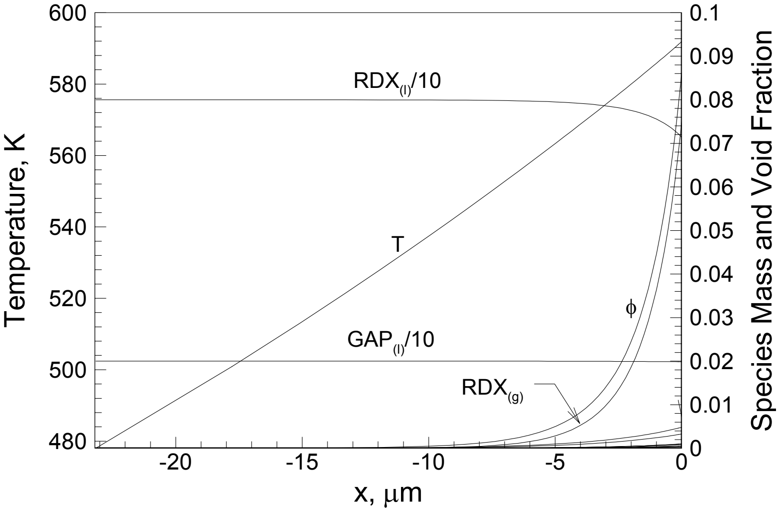

Figure 19. Predicted flame structure in the foam layer of RDX/GAP pseudo propellant (mass ratio 8:2) at 1 atm and laser intensity 100 W/cm$^2$.

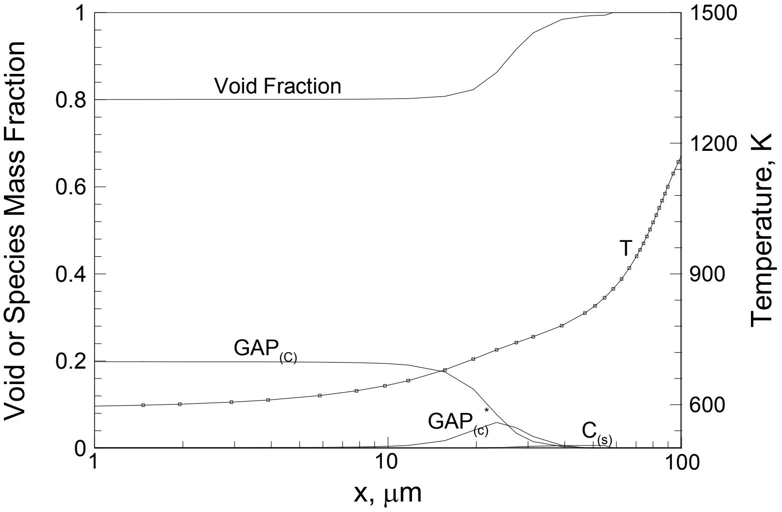

Figure 20. Predicted temperature, void fraction, and condensed species concentration profiles in the near surface region of RDX/GAP pseudo propellant (mass ratio 8:2) at 1 atm and laser intensity 100 W/cm$^2$.

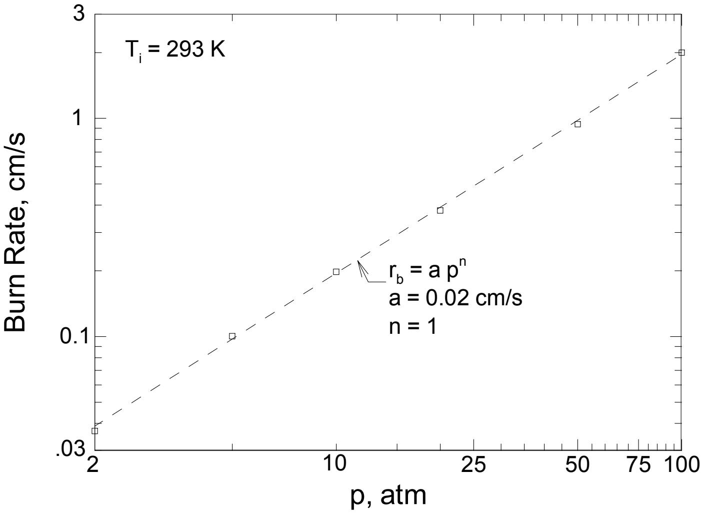

Figure 21. Predicted pressure dependence of burning rate of RDX/GAP pseudo propellant (mass ratio 8:2).

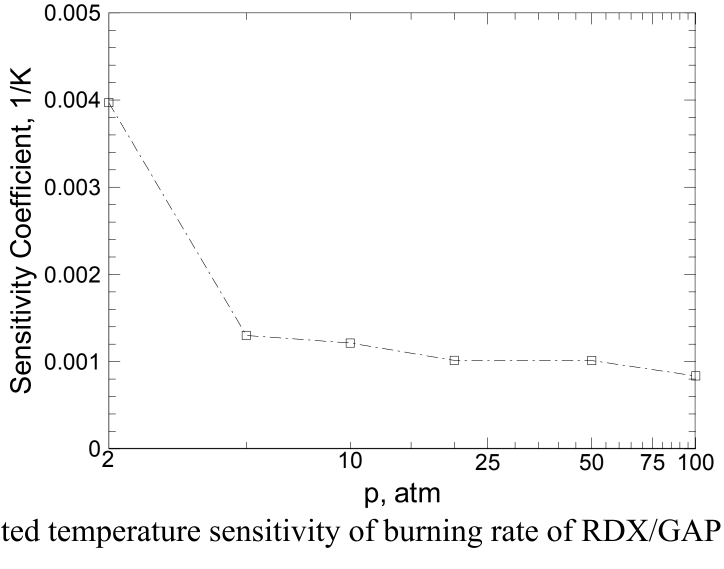

Figure 22. Predicted temperature sensitivity of burning rate of RDX/GAP pseudo propellant (mass ratio 8:2).

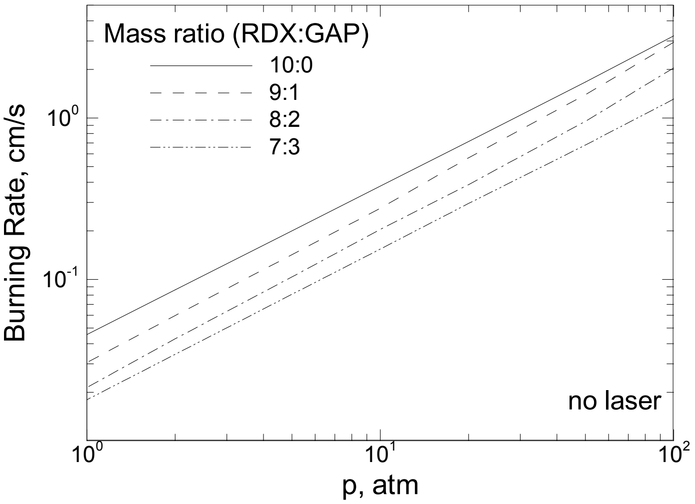

Figure 23. Predicted effect of propellant formulation on burning rate at various pressures.

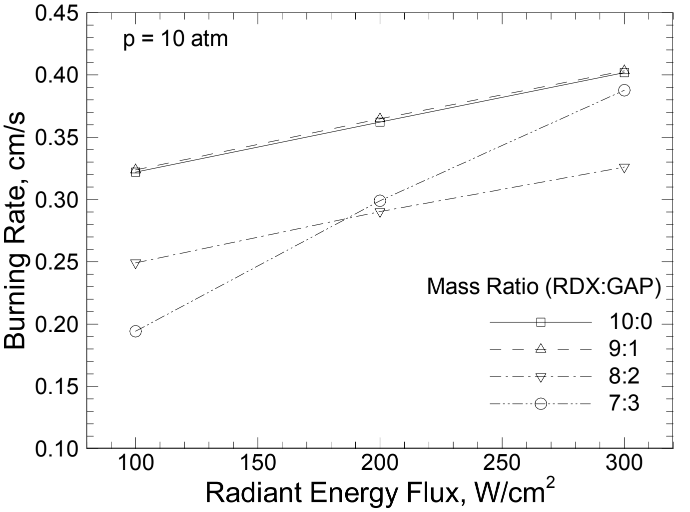

Figure 24. Predicted effect of propellant formulation on burning rate at various laser and composition levels.